DEPARTMENT OF PHYSICS
UNIVERSITY OF JYVÄSKYLÄ
RESEARCH REPORT No. 6/2001

STUDIES OF NEUTRON-RICH NUCLEI CLOSE TO MAGICITY

BY
SAARA NUMMELA

Academic Dissertation
for the Degree of
Doctor of Philosophy

Jyväskylä, Finland
June 2001

DEPARTMENT OF PHYSICS
UNIVERSITY OF JYVÄSKYLÄ
RESEARCH REPORT No. 6/2001

STUDIES OF NEUTRON-RICH NUCLEI CLOSE TO MAGICITY

BY
SAARA NUMMELA

Academic Dissertation
For the Degree of
Doctor of Philosophy

To be presented, by permission of the
Faculty of Mathematics and Natural Sciences
of the University of Jyväskylä,
for public examination in Auditorium FYS-1 of the
University of Jyväskylä on June 5, 2001
at 12 o'clock

Jyväskylä, Finland
June 2001

URN:ISBN:978-951-39-9477-8
ISBN 978-951-39-9477-8 (PDF)
ISSN 0075-465X

Jyväskylän yliopisto, 2023

ISBN 951-39-0972-7
ISSN 0075-465X

Preface

The experimental studies of this thesis have been carried out during the years 1997-2001 mainly at the Department of Physics, University of Jyväskylä. My warmest thanks are addressed to the whole staff of the Department for creating such a friendly and supporting working environment. I also wish to thank the ISOLDE collaboration at CERN.

I wish to express my thanks to my supervisor Prof. Juha Äystö, who has created a fruitful ground for experimental nuclear physics in the IGISOL group in Jyväskylä. I would like to thank all the group members, especially Dr. Ari Jokinen, Dr. Peter Dendooven, Mr. Jussi Huikari, Dr. Gerard Lhersonneau, Mr. Arto Nieminen, Mr. Zoran Radivojevic and Mr. Sami Rinta-Antila. One could not wish for a more pleasant and able team to work with. I am also grateful to Dr. Pauli Heikkinen and Dr. Valerie Rubchenya for valuable discussions.

It has been a great pleasure to work with our collaborators from Strasbourg. The role of Prof. Guy Walter has been invaluable for this work and I wish to express my gratitude to him, and his colleagues in Strasbourg, for an inspiring and rewarding collaboration. Special thanks belong to Dr. Frederic Nowacki and Dr. Etienne Caurier, for providing the shell model calculations, and to Dr. Paule Baumann and Dr. Albert Knipper for their strong contribution on the publications.

The financial support from the Graduate School of Particle and Nuclear Physics and the Vilho, Yrjö and Kalle Väisälä Foundation is gratefully acknowledged.

Finally, I would like to thank my family for their encouragement throughout my studies. I also wish to thank my dear husband, Jyri, for his support during these years.

Jyväskylä, May 2001

Saara Nummela

Abstract

This thesis deals with the experimental study of exotic neutron-rich nuclei. Three N~20 nuclei close to the so-called island of inversion have been studied via beta decay at the ISOLDE facility at CERN. The low energy level scheme of ^{34}Si (N=20) has been confirmed and the first level schemes for ^{35}Si (N=21) and ^{33}Mg (N=21) have been proposed. Single particle energies for ^{35}Si have been determined according to which the effective interaction in the *sd-fp* shell-model has been modified and comparison between theory and experiment is given for different neutron-rich isotopes. The ground state of ^{33}Mg has been assigned as $J^{\pi}=3/2^{+}$, manifesting the inversion of states in the island of inversion.

In addition, superasymmetric fission yields have been obtained for 30 MeV proton induced fission of ^{238}U at the IGISOL mass separator facility at the Accelerator Laboratory of the University of Jyväskylä. A velocity filter has been designed and built in connection with the IGISOL beam line in order to separate double charged ions.

Contents

1 Introduction

The systematic study of the beta decay properties of exotic nuclei far from the valley of stability is essential for understanding the nuclear structure. Except for the lightest elements up to oxygen the boundary of the experimentally reached region of neutron-rich nuclei is still far away from the neutron drip line, which leaves a great challenge for experimentalist for years to come. Not only this urges on the development of new powerful methods to produce and detect such nuclei but also it makes sure that the progress in diverse nuclear models remains active.

Although the number of undiscovered bound nuclei is still very large on the neutron-rich side, thus offering us an almost endlessly large site, we are able to make single big steps by studying just few specific nuclei, so-called key nuclei. These nuclei act as milestones in establishing the new effects that arise in extreme conditions of isospin asymmetry. By rephrasing this, the nuclear models as we see them today are evolved based on the available experimental data, which leads to the fact that in many cases the model parameters simply are insufficient in predicting nuclear features that appear closer to the drip line. Such an example of a characteristic feature is the magicity of the nucleon number in a nucleus. Whereas the nuclear shell model was built around the concept of well-defined magic numbers, the experimental investigation has proven that the magicity of certain nucleon numbers may break far from stability.

The general outline of this thesis is composed of two topics. The first theme is the spectroscopic study of three beta-decaying nuclei around the so-called "island of inversion", for which measurements at the ISOLDE mass separator facility, CERN, were performed. The second theme concentrates on superasymmetric fission yield measurements at the IGISOL facility in Jyväskylä and the design of a velocity filter. Although the two topics might seem at first somewhat unconnected, they both eventually share a common interest, that is to study key-nuclei that reflect the evolution of magic numbers in neutron-rich nuclei.

The main weight is kept on the first-mentioned topic, namely on the spectroscopy of beta decaying neutron-rich nuclei, ^{34}Al, ^{35}Al and ^{33}Na, and the construction of the energy level scheme for their daughter nuclei ^{34}Si, ^{35}Si and ^{33}Mg, respectively. These nuclei are located around the N=20 shell closure, a region where strong deformation has been detected. This unexpected phenomenon was explained by the inversion in *sd-fp* shell ordering across the N=20 shell closure, thus introducing in the calculations neutron excitations from the *sd* shell into the *fp* major shell, which again lead to deformed ground state configurations. A better understanding of the shell ordering and the effective interaction requires experimental data. The interplay between normal ($0\hbar\omega$) and intruder ($1\hbar\omega$,$2\hbar\omega$) excitations can be studied for example with Si (Z=14) nuclei through the observation of 0^+ and 2^+ states. This was the case in our study of the ^{34}Si (N=20) level scheme, which we hoped to complement by observing the excited 0^+_2 state. The study of the ^{35}Si nucleus (N=21), which can be referred as a key-nucleus, provided new information on the evolution of neutron orbits outside the N=20 closed shell. This offered the next step in N=21 systematics, starting from the well known single particle spectrum of ^{41}Ca. Furthermore, the investigation of the ^{33}Mg (Z=12, N=21) level scheme was a logical step in the N=21 systematics and answered our question whether this nucleus lies inside the island of inversion. In Figure 1.1 a part of the nuclide chart is shown and the island of inversion is pointed out by a hatched region. However, the edges of the region are not yet established and the presented limits are only expectations by shell model calculations.

The second topic is related to the study of neutron-rich nuclei around doubly-magic ^{78}Ni (Z=28, N=50). It would be intriguing to find what effect such a large excess of neutrons might have on the structure of ^{78}Ni. Although a great deal of effort has been put on the search for ^{78}Ni in several laboratories, yet no spectroscopic study has been possible due to low production yields. The superasymmetric fission has proven to be a powerful method to produce nuclei in this mass region and the yield measurements at IGISOL aim to predict the usability of such reactions in the spectroscopic study of nuclei close to ^{78}Ni. Therefore, superasymmetric fission yields of 30 MeV proton induced fission of ^{238}U were measured and compared with theoretical calculations and data from other facilities. In

order to achieve an efficient and clean detection of fission products, a Wien velocity filter was designed and built in connection with the IGISOL beam line. Together with a cooler device, this would enable us to eliminate and separate the disturbing doubly charged reaction products, which in some cases severely hinder the detection of the fission products of 70<A<80. Tests concerning the performance of such a device and the charge exchange process in the ion cooler will be presented.

Finally, one could say that the ultimate purpose of the above described studies, as it should be for any experimental nuclear structure study in general, is to provide means to extract the *basic physics phenomena* that emerge from an inspection of nuclear data or that lie behind the results of nuclear model calculations. This goal is in no way trivial and it calls for a systematic and large scale investigation of numerous nuclei, each of which eventually outlines the big picture composed of the fundamental interactions in nature.

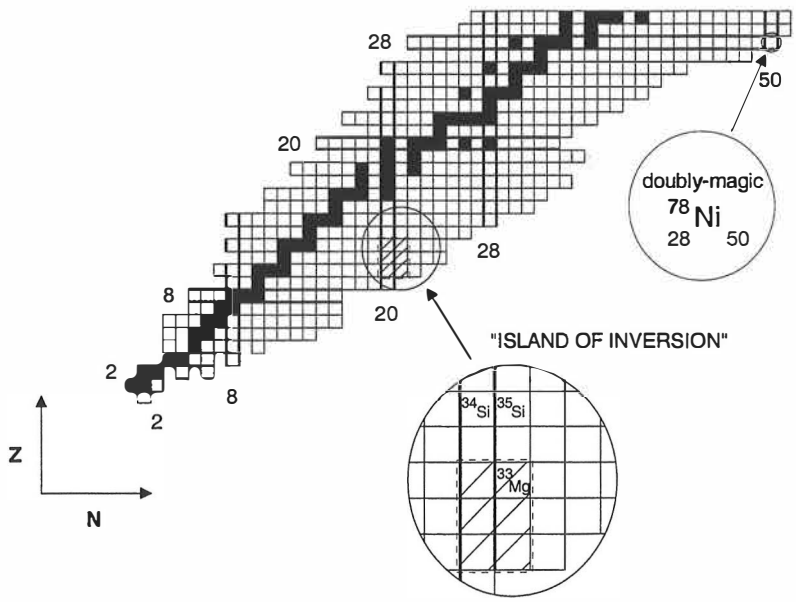

Figure 1.1. Part of the nuclide chart; the region of "island of inversion" and the doubly-magic nucleus ^{78}Ni.

This thesis is based on the following Publications:

1. ***Production of neutron-rich nuclei with A<80 in superasymmetric fission at IGISOL*** https://ui.adsabs.harvard.edu/abs/1999AcPPB..30..677H/abstract

   S. Hankonen*, P. Dendooven, J. Huikari, A. Jokinen, V. Kolhinen, G. Lhersonneau, A. Nieminen, K. Peräjärvi, V.A. Rubchenya, W.H. Trzaska, J.C. Wang and J. Äystö.

   Acta Physica Polonica B **30** (1999) 677.

   * At present known as S. Nummela

   https://www.researchgate.net/publication/260879722

2. ***Spectroscopy of ^{34,35}Si by β decay : sd-fp gap and single-particle states***

   S. Nummela, P. Baumann, E. Caurier, P. Dessagne, A. Jokinen, A. Knipper. G. Le Scornet, C. Miehé, F. Nowacki, M. Oinonen, Z. Radivojevic, M. Ramdhane, G. Walter, J. Äystö and the ISOLDE Collaboration,

   Phys. Rev. C **63** (2001) 044316.
   https://doi.org/10.1103/PhysRevC.63.044316

3. ***Intruder features in the island of inversion: The ^{33}Mg case***

   S. Nummela, F. Nowacki, P. Baumann, E. Caurier, J. Cederkäll, S. Courtin, P. Dessagne, A. Jokinen, A. Knipper, G. Le Scornet, L.G. Lyapin, C. Miehé, M. Oinonen, E. Poirier, Z. Radivojevic, M. Ramdhane, W.H. Trzaska, G. Walter, J. Äystö and the ISOLDE collaboration,

   Phys. Rev. C, submitted.
   https://doi.org/10.1103/PhysRevC.64.054313

4. ***Wien filter for cooled low-energy radioactive ions beams***

   S. Nummela, P. Heikkinen, J. Huikari, A. Nieminen, A. Jokinen, S. Rinta-Antila, V. Rubchenya and J. Äystö,

   Nucl. Instrum. and Meth. A, submitted.
   https://doi.org/10.1016/S0168-9002(01)01362-6

2 Theoretical framework

There exists a large variety of experimental information about the atomic nuclei, such as masses or binding energies, nucleon separation energies, decay and excitation schemes with energies, angular momenta and parity of states, half-lives and various reaction data. All these are obtained by diverse arrays of experimental and theoretical methods. In this work, the information on the nuclear structure is obtained through the beta decay and the nuclear level schemes analysed in the shell model framework. The experimental data act as input parameters for shell model calculations, which contribute to the basic physical quantities, such as nucleon interactions, for a specific range of nuclei.

2.1 Shell model description

2.1.1 *Basics of the shell model*

If we look at gross nuclear properties, such as nucleon separation energies, we find that these vary relatively smoothly in most regions of the nuclide chart. However, at certain specific nucleon numbers, the so-called magic numbers (2, 8, 20, 28, 50, 82, 126), we observe discrete jumps. These are the fingerprints of the nuclear shell structure. Another example of such traces is the excitation energy of the first excited 2^+ state in even-even nuclei. In doubly magic nuclei, such as ^{40}Ca (Z=20, N=20), this excitation energy is considerably higher compared to the neighbouring nuclei. The magic numbers are also of relevance for the formation of elements in stellar events where intense neutron fluxes exist. The rapid neutron capture, so-called *r*-process, in competition with beta decay is responsible for the formation of heavier nuclei and the role of magic nuclei is to slow down the *r*-process at magic neutron numbers.

The analogy for the nuclear shell structure was found from the atomic physics. Whereas in the atom the electrons orbit around an almost point-like nucleus, forming a spherically symmetrical central potential, the nucleus is a densely packed system in which the nucleons interact through an attractive and short range strong interaction. Therefore, the

choice for a central potential in nuclear case is in no way trivial. However, it turns out that such a potential is applicable also for the nucleus. It is essentially the Pauli principle which allows this concept of independent particle motion.

The general from of the nuclear Hamiltonian is

$$H = \sum_{i=1}^{A} T(i) + \sum_{1=k<l}^{A} W(k,l), \qquad (2.1)$$

where $T(i)$ denotes the kinetic energy terms and $W(k,l)$ stands for the two-body-interactions between nucleons k and l. The starting point of the shell model is the single-particle model [Hax49], based on an independent nucleon orbiting freely in a spherically symmetrical central potential, $U(r)$, produced by all the other nucleons inside the nucleus. The Hamiltonian, describing such independent-particle motion in a nucleus with the total number of A nucleons, is given by

$$H^{(0)} = \sum_{i=1}^{A} [T(i) + U(r_i)], \qquad (2.2)$$

where $U(r_i)$ is the single particle potential. The realistic shell model Hamiltonian includes also the particle-particle correlations, represented by the so-called residual interactions. The Hamiltonian which describes these residual interactions is given by

$$H^{(1)} = \sum_{k<l}^{A} W(k,l) - \sum_{i=1}^{A} U(r_i) \qquad (2.3)$$

so that the total Hamiltoninan H, consisting of the independent particle motion and residual interactions, is

$$H = H^{(0)} + H^{(1)} = \sum_{i=1}^{A} [T(i) + U(r_i)] + \left[\sum_{1=k<l}^{A} W(k,l) - \sum_{i=1}^{A} U(r_i) \right] \qquad (2.4)$$

which can be eventually applied to the many-body Schrödinger equation, $H\Psi = E\Psi$. By considering $H^{(1)}$ as a perturbation in the total Hamiltonian, the expectation value of the Hamiltonian is calculated by using the eigenstates of the unperturbed Hamiltonian, $\Phi_\Gamma^{(0)}$, where letter Γ includes the total spin J and isospin T. The energy of the state is therefore given by

$$E_\Gamma = \left\langle \Phi_\Gamma^{(0)} \middle| H^{(0)} + H^{(1)} \middle| \Phi_\Gamma^{(0)} \right\rangle = \sum_{k=1}^{A} e_{a_k} + \left\langle \Phi_\Gamma^{(0)} \middle| H^{(1)} \middle| \Phi_\Gamma^{(0)} \right\rangle, \qquad (2.5)$$

where the first terms, e_{ak}, result from the single-particle energies and the second term from the residual interaction.

In real shell model calculations the nuclear states are not represented by pure shell-model states, $\Phi_k^{(0)}$. The residual interactions, which strongly contribute to the energy eigenstates, make possible that nucleons may scatter from one state into the other. The actual state is therefore a linear combination of the pure shell model states, expressed as

$$\Psi_p = \sum_{k=1}^{g} a_{kp} \Phi_k^{(0)} . \qquad (2.6)$$

The square of each coefficient, a_{kp}, may be interpreted as the probability that the nucleus is in the state $\Phi_k^{(0)}$. Thus, the complete Hamiltonian and the mixed wavefunction finally result in a matrix form with matrix elements H_{lk}, of which the diagonal matrix elements results from the unperturbed Hamiltoninan, $H^{(0)}$, and two-body interactions. The solution of a nuclear energy spectrum comes finally from diagonalization of the energy matrix.

Concerning the choice of the central potential $U(r)$, a harmonic oscillator potential is frequently used as it appears advantageous from a mathematical point of view. The labelling of shell orbits follows also the oscillator quantum number, N. A more realistic potential, although mathematically less adaptable, is the Woods-Saxon potential. The effect of the Woods-Saxon potential, as compared to the harmonic oscillator, is to remove the l degeneracies of the major shells. Owing to this change in potential, the magic numbers 2, 8 and 20 appear. It was only after the introduction of the strong spin-orbit interaction that all the experimentally observed magic numbers could finally be reproduced by the model. The contribution of this term to the energy of the single-particle states is that the originally degenerate levels $j = l \pm ½$ are split, the $j = l + ½$ level being depressed into the normal parity states of the lower major shell.

2.1.2 *Truncations and residual interactions*

Shell model calculations are performed always in limited configuration space, which consists of a restricted set of single-particle states outside an inert core, often a doubly-

magic nucleus. The choice of a configuration space is crucial since the number of active nucleons and single-particle orbits, as well as the *j*-values of the orbits, determine the size of the matrices involved. On the one hand, one needs to have a large configuration space, in order to account for most part of the real configurations, and, on the other hand, the matrices should be kept in manageable size. One method is to include truncations so that with certain conditions, depending on the truncation method, the model space can be restricted. Another method is the so-called Lanczos method, in which one obtains the eigenvalues and eigenvectors from only part of the full matrix. In this way one does not have to diagonalize the whole matrix.

A direct consequence of truncation is that the residual interactions have to be considered as effective interactions. Whereas a true physical interaction operates on complete configuration spaces, an effective interaction is designed for the truncated configurations, still yielding the same result. Therefore, the effective interaction is dependent on the particular model space and the appropriate choice for such a nucleon-nucleon interaction is not trivial. In general, the interaction matrix elements for an n-particle system can be expressed as a linear combination of two-body matrix elements, where the two-body operator is of the form

$$H^{(1)} = \sum_{i<k=1}^{n} V(i,k)\,. \qquad (2.7)$$

There are three different approaches for defining such matrix elements. One is the so-called empirical approach which takes the interaction matrix elements as free parameters in a chosen configuration space and fits them to experimental spectra. An example of such an interaction is the USD (Universal SD-shell) matrix element [Wil84], which has been successfully used for the interactions in the *sd* shell. There are also the so-called realistic interactions, which start from the free nucleon-nucleon interaction. The parameters of the free nucleon-nucleon interaction are obtained by fitting some free nucleon-nucleon scattering observables and further modified to obtain appropriate nuclear two-body interaction matrix elements. Referring to the shell model calculations specifically used for the nuclei studied in this work, the KB' matrix elements [Pov81] and G matrix of Kahana, Lee and Scott [Kah69] represent such realistic interactions. Finally,

so called schematic interactions, such as surface delta interaction (SDI), use more simple nucleon-nucleon forces in order to successfully correlate many observed nuclear properties.

2.2 Validity of the shell model

2.2.1 *Magic numbers in the valley of stability*

When we talk about the experimental confirmation of the magic numbers, we refer to the data close to the valley of stability, as it has been the starting point for any experimental work in nuclear physics. Good examples of magic nuclei in the valley of stability are doubly magic nuclei $^{16}_{8}O_{8}$, $^{40}_{20}Ca_{20}$ or $^{208}_{82}Pb_{126}$, in which both the proton and neutron numbers are magic. They have an extremely high energy of the first excited state and the predominance of negative parity states. In Figure 2.1 the lowest excited states of even ^{40}Ca – ^{48}Ca nuclei, which all are stable, are shown, representing the systematics from one doubly magic nucleus to another.

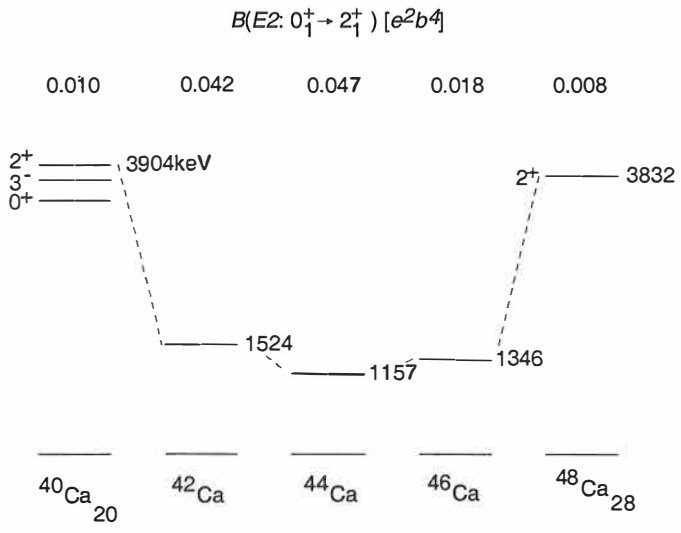

Figure 2.1 Low-lying levels and B(E2) values for the even-even Ca nuclei.

The 2^+ states, as well as *B(E2)* values, clearly demonstrate the effect of closed shells N=20 and N=28 in Ca isotopes. The success of the independent particle model is that the level sequences for nuclei near closed shells can be reproduced extremely well, as it is in ^{41}Ca case where a single neutron is promoted to produce the lowest excited states. The angular momenta *J* of the ground state and of low lying excited states are given directly by the *j* values of the orbits into which the last odd nucleon can be placed.

2.2.2 *Magic numbers far from the stability*

The shell model approach near the valley of stability relies heavily on the concept of closed shells and the strength of magic numbers. However, the situation becomes somewhat more complicated when we approach the nucleon drip-lines and the ratio between the number of neutrons and protons becomes extreme. Such an example is the neutron-rich region around the magic number N=20 for elements $10 \leq Z \leq 12$ where unexpected ground state deformation was observed as irregularities in the binding energies more than 20 years ago [Thi75]. The observation could not be explained by shell model calculations in which nucleon excitations are restricted inside the major shells, forming so-called "normal states". Instead, for a proper description another degree of freedom had to be included in the calculations, namely nucleon excitations across the major shells. Such an excitation of two neutrons across the N=20 major shell is illustrated in Figure 2.2. This approach has been successfully used both in Hartree Fock calculations [Cam75] and in shell model calculations [Wat81, Wil83, Pov94, War90, Hey91, Fuk92, Ots96, Ret97, Cau98]. These so-called "intruder configurations" are in competition and coexist with the normal states of the nucleus and in some specific cases the states may be inverted so that the ground state is dominated by an intruder configuration. Such an inversion is an indication of the vanished N=20 shell closure in the very neutron-rich region and can be observed as deformed configurations. In the N=20 case the region has been named as "the island of inversion".

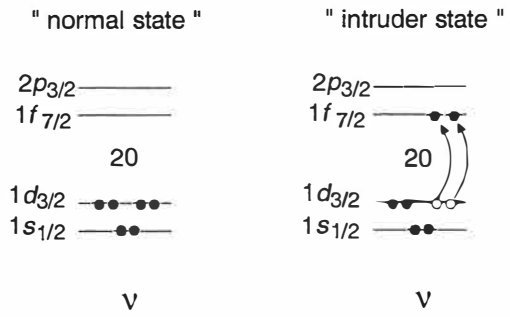

Figure 2.2. A normal state, 0ħω, for N=20 neutrons (left) and an intruder state, 2ħω, via excitation of two neutrons (right).

The development of calculations concerning the island of inversion has gone forward hand in hand with diverse experimental investigations. Mass measurements of heavy Mg isotopes [Det79] revealed the shape transition from spherical to prolate shapes at N=20. Subsequent mass measurements [Gil87] of neutron-rich isotopes in the N=20 region confirmed the excess binding in Na isotopes. Beta decay measurements of Na isotopes [Gui84, Klo93] have enabled the study of low energy level schemes of some neutron-rich Mg isotopes, such as ^{32}Mg, mapping the limits of the island of inversion. In addition, the beta-decay study of ^{34}Al [Bau89] introduced the double-magicity of ^{34}Si (Z=14, N=20), which shows that the nucleus in question lies outside the island of inversion.

Coulomb excitation at intermediate energies has provided a powerful tool in studying the *B(E2)* values of the low lying states of nuclei far from the stability line. Such a study at Riken [Mot95] resulted for ^{32}Mg(Z=12, N=20) a B(E2:$0_1^+ \rightarrow 2_1^+$) value of 454±78 e^2fm^{2L}, which confirms a large deformation for ^{32}Mg suggested by the low excitation energy of the 2^+ state. Furthermore, recent investigations through in beam Coulomb excitation at NSCL [Ibb98, Ibb99] have allowed a systematic study of B(E2; $0_1^+ \rightarrow 2_1^+$) values for even $^{32\text{-}38}$Si nuclei, revealing the quadrupole collectivity of these isotopes. These measured *B(E2)* values could be reproduced by calculations by assuming N=20 as a closed shell for Si isotopes. The clear cut from a spherical ground state shape to the deformed shape is illustrated in Figure 2.3, where the 0_1^+ ground state and 2_1^+excited

state are shown for ^{34}Si and ^{32}Mg, together with their corresponding $B(E2; 0_1^+ \rightarrow 2_1^+)$ values.

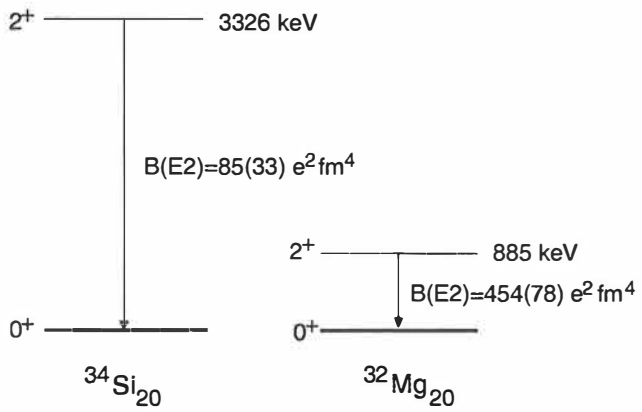

Figure 2.3. The 0_1^+ ground state and 2_1^+ excited state of ^{34}Si and ^{32}Mg. The $B(E2; 0_1^+ \rightarrow 2_1^+)$ values of ^{34}Si and ^{32}Mg are taken from ref. [Mot95] and [Ibb98], respectively.

Subsequent Coulomb excitation studies at NSCL [Pri00a, Pri00b] have enabled the first observation of an excited state in ^{31}Na, which corresponds to a rotational excitation built on a strongly deformed ground state. They also revealed excited states in ^{33}Si and ^{34}P, which appear to have spherical shapes and thus are located along the boundary of the island of inversion. Very recently, another nucleus expected to be located at these boundaries, namely ^{34}Al, has been studied with similar experimental methods [Pri01].

The beta decay half-lives have been measured with a Time-Of-Flight Isochronus spectrometer, resulting on $T_{1/2}$ information on ^{34}Al and ^{35}Al, as an example [Ree95]. Recent mass measurements at GANIL [Sar99, Sar00] for neutron-rich $29<A<47$ nuclei have indicated that around N=28 the ground states would be described by prolate deformations. In addition, evidence for shape coexcitence was provided in these measurements by the observation of an isomer in ^{43}S.

The study of exotic N=50 nuclei, both on the neutron-rich and neutron-deficient side, is one of the most intriguing subjects in experimental nuclear physics of today. On the neutron-deficient side the ^{100}Sn nucleus is the heaviest doubly-magic N=Z nucleus which

is bound and can be synthesised, and offers the possibility to test the shell model where protons and neutrons occupy the same orbits. However, so far the ^{100}Sn nucleus has only been identified [Lew94]. The ^{78}Ni nucleus, on the other hand, would test the magicity of the N=50 shell closure on the very neutron-rich side and would shed light on the astrophysical *r*-process, which is partly responsible for the production of nuclei with A<70. So far, the spectroscopic study of ^{78}Ni has been out of experimental reach and the production rates have allowed only the mere identification of few of these nuclei [Ber95]. Therefore, no test for theories concerning the double-magicity of ^{78}Ni has been available.

2.3 The "island of inversion"

The discussion of the results in the present work is based on shell model calculations by F. Nowacki and E. Caurier. They use a valence space of the full *sd*-shell for Z-8 protons and the *sd*- and *pf*-shells for the neutrons. In other words, the interaction is defined on top of an ^{16}O core. The nuclear states are formed either by 0hw, 1hω or 2hω neutron excitations, corresponding to excitations inside the major shell *(pf)* or from *sd*- to *pf*-shell, respectively. The protons remain in the *sd*-shell, as demonstrated in ref. [Cau98]. The effective interactions used in this work are the USD interaction of Wildenthal [Wil84] for proton-proton interaction in the *sd*-shell, KB' (Kuo-Brown) matrix elements [Pov81] for the neutron-neutron interaction in the *pf* shell and the G matrix of Lee, Kahana and Scott [Kah69] for the cross shell neutron-proton interaction. These interactions have been introduced in ref. [Ret97]. As already mentioned, the construction of the effective Hamiltonian is the crucial part of the shell model. In order to determine the interaction involved, the calculations need experimental data of some so-called "key-nuclei". This stresses the role of the experimental effort, since in some cases the key-nuclei are scarce and difficult to produce. In this work the interaction, or more precisely some monopole (J=0) parts of the interaction, are obtained from data of four key nuclei. These nuclei, ^{39}K, ^{47}K, ^{41}Ca and ^{35}Si, correspond to simple structures of one particle or one hole in a doubly closed-shell. These structures are schematically shown in Figure 2.4.

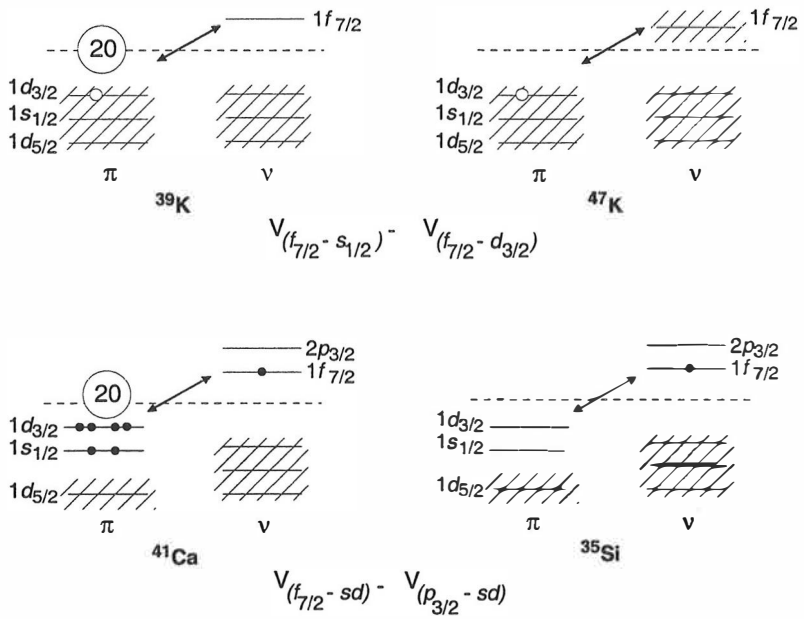

Figure 2.4. Four key nuclei for determining the effective interaction V. In the upper part, proton-hole with neutron filling in K isotopes. In the lower part, neutron-particle evolution with decreasing proton number in N=21 isotones.

In the case of K isotopes, there is a hole in the proton *sd*-shell and the neutron number varies from N=20 to N=28, corresponding to ^{39}K and ^{47}K, respectively. The experimentally obtained evolution of the $3/2^+$ and $1/2^+$ states has fixed the difference between the $f_{7/2}d_{3/2}$ and $f_{7/2}s_{1/2}$ monopoles [Ret97]. Out of the other pair of the key-nuclei, ^{41}Ca and ^{35}Si, the level scheme of the latter was unknown prior this work. These nuclei correspond to configurations with one neutron in the *fp*-shell ($f_{7/2}$ or $p_{3/2}$ orbit), with varying number of protons in the *sd*-shell. Hence, the evolution of the $3/2^-$ excitation ($\nu p_{3/2}$) is reproduced by $p_{3/2}s_{1/2}$ and $p_{3/2}d_{3/2}$ terms. The consequences of the resulting changes in the interaction are discussed later. The experimental study of the ^{35}Si level scheme is therefore well motivated by shell model arguments, as well as for the next even-Z, N=21 nucleus, ^{33}Mg.

In the case of ^{34}Si, which is proven to lie outside the island of inversion [Bau89], the most interesting states from a shell model point of view are the 0^+ and 2^+ states. They can

be either normal (0p-0h) states or intruder (2p-2h) states, depending whether the nucleon pair excitations are inside, or across, the major shell. Experimentally, only the 0_1^+ and 2_1^+ states have been observed in ^{34}Si, corresponding to a 0p-0h ground state and a 2p-2h excited state at 3326 keV. It would be of great interest to fix also the 0_2^+ (2p-2h) state and the 2_2^+ (0p-0h) states. We have to keep in mind that these are not pure states, in a sense that each actual state is always a mixture of both a normal and an intruder state. In other words, if normal states are noted as $\Psi(0\hbar\omega)$ and intruder states as $\Psi(2\hbar\omega)$, the real wave function of the state is

$$\Psi = a\,\Psi(0\hbar\omega) + b\,\Psi(2\hbar\omega), \qquad (2.8)$$

where the coefficients a and b give the percentage of the components. Simply by investigating the experimental decay scheme [Bau89], and noting that there exists a transition 2_1^+(2p-2h) $\rightarrow$ 0_1^+(0p-0h), we conclude that there has to be some finite amount of mixing in both (or either) states. If they would be pure 0p-0h and 2p-2h states, the transition probability would simply vanish. However, a proper amount of mixing brings up the probability for the transition [Cau98].

2.4 Beta decay

The study of beta decay provides a rich source of information on the nuclear phenomena. Not only it acts as a means to produce nuclei in various excited states, not reached by other reactions, but also reveals features of the fundamental weak interaction as a mechanism itself. For a neutron rich nucleus with mass A and charge Z the process can be written as

$$(A,Z) \rightarrow (A, Z+1) + e^- + \bar{\nu}, \ (\beta^- \text{ decay}) \qquad (2.9)$$

where e^- correspond to an electron and $\bar{\nu}$ to an antineutrino. The beta decay is therefore a process through which an exotic nucleus far from stability approaches the valley of

stability via an isobaric chain. For a neutron-deficient nucleus there is a competition between two processes, β^+ decay and electron capture (EC), for which hold

$$(A,Z) \rightarrow (A, Z\text{-}1) + e^+ + \nu \qquad (\beta^+ \text{ decay}) \qquad (2.10)$$

$$(A,Z) + e^- \rightarrow (A, Z\text{-}1) + \nu, \qquad (\text{EC}) \qquad (2.11)$$

where e^+ correspond to a positron and ν to a neutrino. In this work the studied nuclei are all of the neutron-rich type and therefore decay through β^- decay. Unlike the proton drip-line, the neutron drip-line is still relatively far from the borders of the nuclide chart reached by experimentalists.

The beta decay is mediated by the weak interaction between the states of a nucleus exhibiting strong interaction. The interaction Hamiltonian, which can described by a charge-current, contains two coupling constants, G_V and G_A, associated with the vector part and axial-vector part of the charge current, respectively. They both may contribute simultaneously to the beta transition probability, so that

$$\lambda \propto G_V^2 \langle M_F \rangle^2 + G_A^2 \langle M_{GT} \rangle^2, \qquad (2.12)$$

where the matrix elements M_F and M_{GT} are referred to as the Fermi and Gamow-Teller matrix elements, respectively. The square of these matrix elements can be expressed explicitly as [Bru77]

$$\langle M_F \rangle^2 = \left\langle J_f M T_f T_{fz} \left| 1 \sum_{k=1}^{A} t_{\pm}(k) \right| J_i M T_i T_{iz} \right\rangle^2 \qquad (2.13)$$

$$\langle M_{GT} \rangle^2 = \frac{1}{2J_i + 1} \sum_{qM_iM_f} \left\langle J_f M_f T_f M_{fz} \left| \sum_{k=1}^{A} \sigma_q(k) t_{\pm}(k) \right| J_i M_i T_i T_{iz} \right\rangle^2, \qquad (2.14)$$

where T's are isospin quantum numbers, M_T's are isospin projections, J's are the total spins, M's are magnetic quantum numbers of initial and final states, $t_{\pm}$ is an isospin rising/lowering operator and σ_q is the spin operator in its cartesian components (x,y,z).

The selection rules for allowed beta decay can by deduced from the above described matrix elements, according to the unity operator, 1, for the Fermi decay and the spin-isospin operator, $\sigma_q t_{\pm}$, for the Gamow-Teller decay. Both the electron and neutrino have an intrinsic spin of ½ that can be orientated either parallel or antiparallel with respect to each other. In a Gamow-Teller (G-T) decay the electron and antineutrino spins are parallel (total S=1), whereas in a Fermi (F) decay spins are antiparallel (total S=0). The electron and the antineutrino might also carry angular momentum $\boldsymbol{L}$ and therefore the process must satisfy the vector addition rules

$$\boldsymbol{I}_f = \boldsymbol{I}_i + \boldsymbol{L} \qquad \text{Fermi transitions} \qquad (2.15)$$

$$\boldsymbol{I}_f = \boldsymbol{I}_i + \boldsymbol{L} + \boldsymbol{1} \qquad \text{Gamow-Teller transitions} \qquad (2.16)$$

where $\boldsymbol{I}_i$ and $\boldsymbol{I}_f$ refer to initial and final angular momenta. Moreover, the parities associated to the initial and final states are related as

$$\pi_f = (-1)^L \pi_I . \qquad (2.17)$$

In the case of allowed Fermi decay the square of the Fermi matrix element can be rewritten as [Bru77]

$$\langle M_F \rangle = T(T+1) - T_{iz} T_{fz} . \qquad (2.18)$$

In this work, the nuclei under study belong to the Z≈14, N≈20 region, and decay always by the Gamow Teller decay. In the case of allowed Gamow Teller decay the matrix elements cannot be expressed directly in terms of the total isospin. Instead, the extreme single-particle estimate for the square of the GT matrix element can be expressed as

$$\langle M_{GT}\rangle^2_{s.p.} = 6(2j_f+1)\begin{Bmatrix} \tfrac{1}{2} & \tfrac{1}{2} & 1 \\ j_i & j_f & l \end{Bmatrix}^2 \qquad (2.19)$$

The actual matrix elements in a many body system are then obtained by summing the single-particle matrix elements over the different configurations.

These selection rules and the decay rates of Fermi and Gamow-Teller decay can further serve as tool to get insight in I^π of the levels. The decay constant of the allowed decay can be written as

$$\lambda = \frac{\ln 2}{t_{1/2}} = \frac{g^2|M_{fi}|^2}{2\pi^3\hbar^7c^3}\int_0^{p_{max}} F(Z',p)p^2(Q-T_e)^2\,dp\,, \qquad (2.20)$$

where the integral is known as Fermi integral. Consequently, the $ft_{1/2}$ value, or the comparative half-life, of an allowed beta transition is deduced as

$$ft_{1/2} = \frac{C}{\langle M_F\rangle^2 + \left(\frac{G_A}{G_V}\right)^2\langle M_{GT}\rangle^2}\,, \qquad (2.21)$$

where constant C = 6145(4) s [Tow95] and f is the so-called statistical rate function (corresponding to the Fermi integral in the simplest case). The Fermi integral can be found tabulated according to particular daughter nucleus (Z_f) and the end point energy (E_{max}).

The usefulness of the experimentally deduced $ft_{1/2}$ value rests on the fact that it depends solely on the nuclear structure and not on the lepton kinematics. The beta decays can be classified by their $ft_{1/2}$ values, or more conveniently by their logarithms $\log ft_{1/2}$. Table 2.1 summarises the beta decay selection rules by classifying the transitions according to their L value and corresponding $\log ft$ limits. The fastest transition is the L=0 transition, which

is called an allowed decay. The higher L values correspond to forbidden decays, which are much less probable than the allowed decays and correspond to longer half-lives.

Table 2.1. Selection rules and logft values for various beta-transition types [Kan95]. Those ΔI values which are not possible if either the initial or the final spin is zero, are in parenthesis. The Fermi integral has been calculated for allowed decay.

Transition Type	*log ft*	*L*	Fermi		Gamow-Teller	
			ΔI	Δπ	ΔI	Δπ
Allowed	<5.9	0	0	No	(0), 1	No
1st forbidden	>8.0[a]	1	(0), 1	Yes	0, 1, 2	Yes
2nd forbidden	≈13	2	(1), 2	No	2, 3	No
3rd forbidden	≈18	3	(2), 3	Yes	3, 4	Yes

[a]The Fermi integral has been calculated for first forbidden decay.

2.5 Beta-delayed neutron emission

Beta decay populates either the ground state or the excited states of the daughter nucleus, which again can be deexcited by gamma emission. However, if the resulting excitation energy is high enough and exceeds the separation energy of one, or more, nucleons in the daughter nucleus there can occur an emission of prompt nucleons. In the case of exotic nuclei far from the valley of stability, the decay energies become large and the energy window above the nucleon separation energy increases. Consequently, the probability for beta-delayed nucleon emission gets higher. As the tendency in nuclear physics today is towards the nucleon drip lines, the study of nucleon emission cannot be omitted. In order to determine experimentally the beta decay strength distribution, and thus determine i.e. the log *ft* values, the fraction of nucleon emission out of the total strength must be included. Moreover, by observing emitted nucleons and their energy spectra, we learn about levels with high excitation energy.

In the present work the nuclei under study are neutron-rich and therefore can undergo beta-delayed neutron emission if

$$E_x > S_n \,, \tag{2.22}$$

where E_x is the excitation energy of the daughter nucleus in β^- decay and S_n is the one-neutron separation energy. Consequently, emission of more than one neutron, let us say k neutrons, is energetically possible if $E_x > S_{kn}$, where S_{kn} is the k-neutron separation energy. In Figure 2.5 the Q_{β^-} values for Na, Mg and Al isotopes are shown, together with the one-neutron and two-neutron separation energies of the corresponding daughter nuclei.

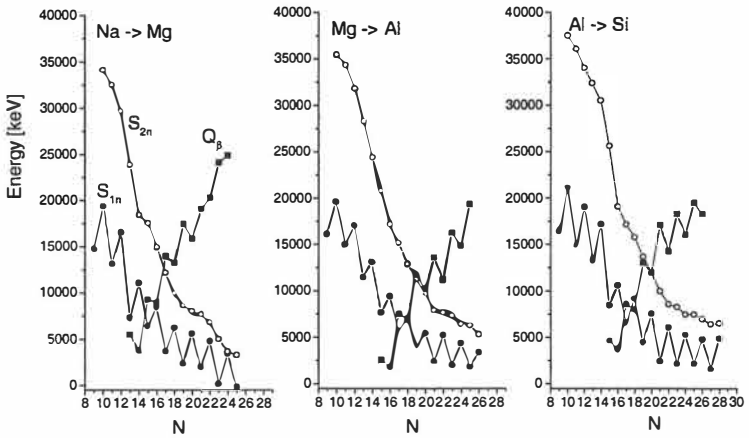

Figure 2.5. The Q_{β^-} values are shown for sequences of Na, Mg and Al isotopes as a function of neutron number (squares). The one-neutron (S_{1n}) and two neutron (S_{2n}) separation energies for their daughter nuclei are illustrated as open and solid circles, respectively. The data are obtained from mass excess values given in ref. [Aud97]

Since the neutron is electrically neutral it is not effected by the Coulomb barrier. Instead, the neutron has to penetrate only the angular momentum barrier in order to be emitted. The height of the barrier increases with increasing angular momentum l of the neutron, proportional to $l(l+1)$, thus favouring the emission of neutrons of low l. The beta-delayed neutron emission channel can also serve as a useful spectroscopic tool, because the change in spin and parity between the initial and final states for $l \neq 0$ decay can be greater compared to the direct beta decay. Experimentally, the beta delayed neutron emission

probability P_n is defined as the number of emitted beta delayed neutrons *per* 100 beta decays.

2.6 Electromagnetic transitions

The main source of experimental information about the spin assignment of nuclear states are the electromagnetic transitions between levels. The conservation laws require that the angular momentum of the initial state, $\boldsymbol{J}_i$, should be equal to the sum of the angular momentum $\boldsymbol{L}$ carried by the emitted radiation and the angular momentum of the final state, $\boldsymbol{J}_f$. This reads

$$\boldsymbol{J}_i = \boldsymbol{J}_f + \boldsymbol{L} \tag{2.23}$$

which defines a selection rule, so called triangle condition

$$\left|J_i - J_f\right| \leq L \leq J_i + J_f \,. \tag{2.24}$$

The conservation of parity defines the following important selection rule for electric and magnetic radiation

$$\begin{aligned} \pi(EL) &= (-1)^L \\ \pi(ML) &= (-1)^{L+1} \,. \end{aligned} \tag{2.25}$$

A useful quantity to connect experimental decay rates and results from model calculations is the reduced transition probability, *B(EL)* and *B(ML)* for electric and magnetic cases, respectively. The reduced transition probability is given as

$$B\left(\varpi L; J_i \rightarrow J_f\right) = \frac{\left\langle J_f \left\| O(\varpi L) \right\| J_i \right\rangle^2}{2J_i + 1} \,, \tag{2.26}$$

which is usually expressed in units e^2fm^{2L}. The relationship between the transition rate $\lambda(\gamma)[s^{-1}]$ and $B(\omega L)$ is shown in Table 2.2. The most important $B(\omega L)$ is the $B(E2)$, which gives insight to the quadrupole moment of the nucleus and therefore on the deformation.

Table 2.2. Relationship between transition rate $\lambda[s^{-1}]$ and B(L). Gamma transition energies are given in MeV, B(EL) in e^2fm^{2L} and B(ML) in $\mu_N{}^2fm^{2L-2}$[Kan95].

L	λ(EL)	λ(ML)
1	$1.59 \cdot 10^{15}\ E^3\ B(E1)$	$1.56 \cdot 10^{13}\ E^3\ B(M1)$
2	$1.22 \cdot 10^{9}\ E^3\ B(E2)$	$1.35 \cdot 10^{7}\ E^5\ B(M2)$
3	$5.67 \cdot 10^{2}\ E^7\ B(E3)$	$6.28 \cdot 10^{0}\ E^7\ B(M3)$
4	$1.69 \cdot 10^{-4}\ E^9\ B(E4)$	$1.87 \cdot 10^{-6}\ E^9\ B(M4)$

3 Experimental methods to study nuclei near N=20 and N=50

The experiments of this work were performed at two different mass separator facilities. The two measurements, concerning the study of the beta-decay of $^{34-35}$Al and ^{33}Na nuclei, were made at the ISOLDE mass-separator facility at CERN in Geneva. The superasymmetric fission yield measurements were performed with the IGISOL mass-separator at JYFL in Jyväskylä, which also included test measurement for a Wien velocity filter. The nature of these experiments differs slightly from each other, which is usually the case for nuclear structure vs. yield measurements. However, in both experiments the basic methods and tools of nuclear spectroscopy are used, although with diverse approaches.

3.1 ISOL technique

The idea of the Isotope Separator On-Line (ISOL) technique is to produce clean mass separated beams of rare radioactive isotopes in a continuous process. The common operating principals of all ISOL systems are stopping, acceleration and mass separation of the reaction products. The main operational differences between various ISOL techniques, however, are concentrated on the stopping of the reaction products and the following ionisation process, required for the acceleration stage. The performance of the device depends mostly on these two things and, as a consequence, the devices can be usually rated according to the selectivity of the desired reaction products and the efficiency and fastness of the whole separation process. In the following text two mass-separator facilities, ISOLDE and IGISOL, will be discussed in more detail.

3.1.1 ISOLDE facility at CERN

In the ISOLDE separator at CERN radioactive nuclei are produced in spallation, fission or fragmentation reactions with a thick target placed in a proton beam of 1 GeV [Kug92], (now even 1.4 GeV), provided by the PS Booster. In the PS Booster four small synchrotrons reaccelerate protons, delivered by a Linac, up to 1.0-1.4 GeV after which

the protons are injected into the CERN Proton synchrotron (PS). The PSB delivers every 1.2 seconds a pulse of $3.2 \cdot 10^{13}$ protons. Up to half of the pulses in the 12 pulses long super cycle is brought to bombard the ISOLDE target, which in the present experiments resulted in an average beam current above 2 μA.

The most crucial parameters concerning the operation of ISOLDE are related to the target and the ion source. Ideally, the reaction products should leave the target fast (i.e. short release time) and the ion source should efficiently produce an ion beam, preferably containing for the most part the isotopes of the studied element. The development work is therefore closely related to chemistry. In the present work, the $^{34\text{-}35}$Al and ^{33}Na isotopes were produced by using a Uranium Carbide target with a thickness of 46 $g \cdot cm^{-2}$ and the reaction products were ionized in a tungsten surface-ionization source. In the mass range $33<A<35$ this target-ion-source combination produces essentially Al isotopes whereas Na isotopes give a minor contribution to the radioactive beam. Other two possible ion-sources at ISOLDE are plasma- and laser-ion-sources.

The release behaviour constitutes of the diffusion of the reaction products from the target material, surface desorption and effusion to the ion source outlet [Let97]. These processes create a certain time structure for the separator beam. The release of a given element from the target can be expressed with a three-component exponential function which expresses the probability density for an atom generated at t=0 of a given element to be released at a time t

$$P(t) = \frac{1}{Norm}\left(1 - e^{-\lambda_r t}\right)\left[\alpha e^{-\lambda_f t} + (1-\alpha)e^{-\lambda_s t}\right], \qquad (3.1)$$

where α is a weighting parameter and the subscripts r, f, and s correspond to time-constant-like parameters of fast rise and fast and slow decay, respectively. The release is independent of the decay losses, and therefore the probability density for a radioactive ion with a decay constant λ_i to be released and not decayed at a time t can be expressed as

$$P(t, \lambda_i) = P(t)e^{-\lambda_i t} \qquad (3.2)$$

The ISOLDE targets serve two different isotope separators, namely GPS (General purpose separator) and HRS (High resolution separator). With the HRS one single mass can be separated with a resolution of M/ΔM=5000, enabling even isobaric purification. In the present two experiments the radioactive beam from the target was separated with the GPS, which has a mass resolving power of M/ΔM=2400. In the first experiment the yield at the detection point for mass separated ^{34}Al was 30 atoms/s while for ^{35}Al it was close to 10 atoms/s. In the second experiment a typical yield was 2 atoms/s for ^{33}Na and 8 atoms/s for ^{35}Al. Both ISOLDE experiments were performed using basically the same measurement geometry in which the mass-separated ions were collected onto a tape which was moved typically once every 10th proton pulse. The production rates for some Na and Al isotopes, measured in the second experiment, are given in Table 3.1. The values are corrected with the transmission of the beam line, the beam-gate period (including the release behaviour of the target) and the tape movement.

Table 3.1. ISOLDE production rates of Na and Al isotopes.

Na isotope	Production rate [at/μC]	Al isotope	Production rate [at/μC]
^{30}Na	80100(20000)	^{33}Al	990(250)
^{32}Na	560(140)	^{34}Al	135(24)
^{33}Na	52(13)	^{35}Al	100(40)

The time structure of the ISOLDE beam is built on the proton pulses, the time interval between pulses being a multiple of 1.2. s. The acceleration high voltage of 60 kV is brought to zero 35 μs before the proton beam impact and restored to its normal value after 6 ms. This pulsed power supply avoids the unnecessary load on the acceleration voltage from the intense ionisation in the air during the beam impact. Followed by the proton pulse, the beam of accelerated radioactive ions is driven through the separator for a certain time, so-called "beam gate", and then cut off until the next proton pulse. The beam gate should be long enough in order to make sure that the studied element has been sufficiently released from the target. On the other hand, the beam gate should not be too

long so that during the pure decay period (beam gate off) one can still observe the radioactive decay of the short-lived isotope under study. During the measurement of ^{34}Al ($T_{1/2}$=55.3 ms) and ^{35}Al ($T_{1/2}$=38.6 ms) we used a beam gate of 100 ms whereas for ^{33}Na ($T_{1/2}$=8.0 ms) we used a beam gate of 20 ms. The time structure of the ISOLDE beam is shown in Figure 3.1. The number of proton pulses during a 14.4 s supercycle varied from 6 to 11.

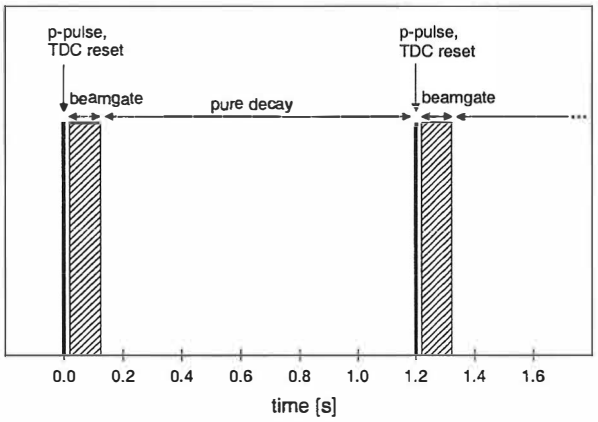

Figure 3.1 Time structure in the ISOLDE experiment.

3.1.2 Detection set-up at ISOLDE

The detector set-up, which is schematically shown in Figure 3.2, was designed to observe β-delayed γ rays and neutrons, enabling β–γ, β–γ–γ, β-n and even some β-n-γ coincidences. The activity was implanted onto an aluminized-Mylar tape, which was moved periodically in order to reduce the amount of contaminants and longer-lived daughter activities. A thin cylindrical plastic detector, covering about 70% of the total solid angle around the collection point, was used as a trigger for the events and provided a start signal for neutron time-of-flight measurements. Two large volume Ge detectors were used to detect γ rays, recording both γ singles and coincidences. For a specific level lifetime measurement in ^{35}Si a better time resolution was needed for the β–γ coincidence

which is why the other Ge detector was replaced by a BaF_2 detector. Since the probability for β-delayed neutron emission in $^{34-35}$Al and ^{33}Na is high it was worth while to record β-delayed neutrons. This was done with eight low-threshold neutron detectors of 15% intrinsic efficiency, which were located around the collection point with a flight path of 50.8 cm [Bou96]. The neutron energy was obtained by time-of-flight analysis, in which the start signal was triggered by a beta in the beta-detector, and the stop signal by a neutron in one of the eight modules.

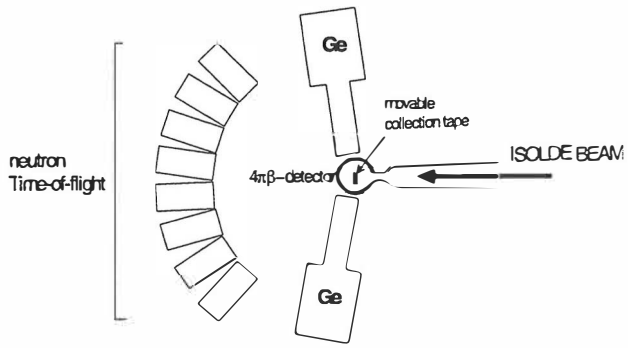

Figure 3.2. Schematic view of the detection set-up used in the ISOLDE experiments.

The data were recorded event-by-event, triggered by a β signal. The energy signals from plastic and Ge detector preamplifiers were amplified by linear amplifiers. The timing signals from Ge detectors were processed by a timing filter amplifiers (TFA) and constant fraction discriminators (CFD), which provided signals for the coincidence unit and stop signals for the time-to-amplitude converters (TAC). The start signal for the TAC was provided by a logic signal from a CFD unit of the beta detector. The energy and time signals were digitised by multichannel CAMAC ADC's and stored on the computer hard disc. A scaler unit, which was set to zero at each proton pulse, provided the time information with respect to the proton impact for each event.

3.1.3 IGISOL facility at JYFL

The Ion-Guide Isotope Separator (IGISOL) technique [Den97] was developed in order to minimise the transport time for the reaction products, as well as to produce ions in a chemically insensitive way. In other words, the aim was to create a fast method to study a large range of rare short-lived (subms) isotopes of various elements [Ärj85]. With the new upgraded IGISOL system at JYFL [Pen97], there have been extensive studies of proton-rich nuclei below A=55 via light-ion induced fission reaction, heavier proton-rich nuclei via heavy-ion reactions as well as neutron-rich nuclei via proton-induced fission, as extensively reviewed in ref. [Äys01]. In the present work, we have concentrated on yield measurements of neutron-rich nuclei in fission [Lei91, Jau94], and more precisely on the production of light fission fragments in the so-called superasymmetric fission mode [Huh97].

The motivation to employ the superasymmetric fission rises from the desire to study exotic neutron-rich nuclei close to Z=28 and N=50. It has been observed that the cross section of proton-induced (E_p=25 MeV) fission of ^{238}U [Huh97] is substantially enhanced relative to thermal-neutron-induced fission of ^{235}U. In order to create conditions as efficient as possible for producing these neutron-rich nuclei, the superasymmetric fission mode has to be well characterised. This requires the study of different beam/target combinations, as well as a usable model that could help to understand the reaction mechanism itself. As a continuation of the previous superasymmetric fission yield measurement by Huhta *et al.*, we undertook a study of 30 MeV proton induced fission of ^{238}U at IGISOL.

The operating principles of IGISOL and ISOLDE differ drastically concerning the target-ion-source approach. At ISOLDE the reaction products diffuse under high temperatures out of a thick target, followed by a separate ionisation step. In order to overcome the difficulties of high melting points (such as Y and Pd), related to severe problems with the ion source, the IGISOL method uses a thin target and gas (He) as stopper for the reaction products recoiling out of the target. As a result, the release is in no way effected by

chemical and physical properties of the element enabling an equally fast process for each element. It is evident that by using gas as a stopper material, compared to a thick target or a solid stopper, we end up with relatively low stopping efficiency. However, the IGISOL technique is still superior when it comes to the study of refractory elements.

Besides the chemical insensitivity, the advantage of IGISOL is that there is no need for a separate ion-source. During the stopping process the initial high charge states of the recoil ions are lowered in He gas typically down to q=1+, although a small fraction ends up as q=2+ ions. A typical He pressure used in the fission ion guide [Den98] is 100-300 mbar, in which small amounts of impurity molecules are added to enhance the charge exchange process if needed. The ions are extracted from the ion guide through an exit hole (nozzle) into a differential pumping system where neutral He gas is evacuated from the target chamber. The q=1+ ions, transported with the He flow, are guided by an electric field through a skimmer system, with a hole diameter of 1.35 mm. The skimmer is followed by the extraction and acceleration stages, which provide a 40 kV acceleration voltage for the ions. The mass analysis is performed by a 55° dipole magnet of the ISOLDE 2 type, which separates the isotopes according to their charge over mass ratio. The mass separated ions can be steered by a deflection system in a focal plane switchyard in three different directions depending on the detector set-up used. The IGISOL beam line and its major components are schematically shown in Figure 3.3.

The yields for superasymmetric fission products were determined by observing γ transitions following the beta decay of the nucleus. Therefore, three Ge detectors (Nordball type [Mos89]) were used, in order to increase the total gamma detection efficiency. The γ rays were recorded in coincidence with betas, which were detected by a cylindrical plastic detector of total efficiency of about 70%. In order to prevent a large fraction of the β's entering the Ge detectors, a 15 mm Plexiglass absorber was introduced between the beta detector and the Ge detectors. The β–γ events were recorded by the VENLA data acquisition system and stored on exabyte tapes.

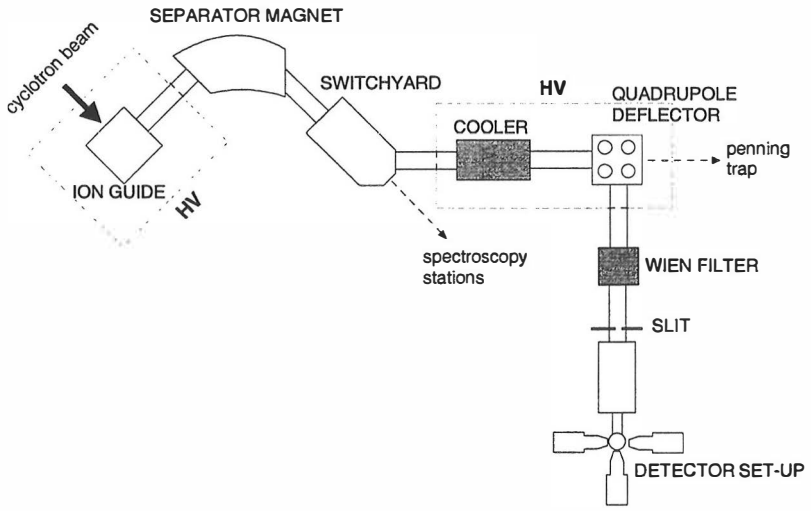

Figure 3.3. Schematic view of IGISOL beam line used in this work.

3.2 Manipulation of ion beams at IGISOL

The operation of the IGISOL mass separator is based on a well known principle of separating ions of equal kinetic energy in a magnetic field according to their charge over mass ratio. Most of the reaction products are extracted from the ion guide as q = 1+ ions, however, a small fraction remains as q = 2+ ions. Therefore, with a given q/m ratio two masses, m=A and m=2A, are lead through the separator. If the production rate for 2A is far higher than for nuclei with mass A, the amount of q=2+ ions become dominant in the mass separated beam. In the case of fission products of A≈70 the cross-section is remarkably larger for the A≈140 nuclei which severely harms the spectroscopic study of the singly charged A≈70 ions. Since it is presently impossible to reduce the amount of doubly charged ions inside the ion guide itself, the charge state of the ions should be lowered after the separator, after which the ions owing to mass A and 2A can be separated with a velocity filter. The charge exchange process can be realised by using the ion cooler in which the q = 2+ charge state can be lowered to q=1+ in proper buffer gas

conditions. In the following two chapters the principles of the cooler and the Wien velocity filter will be discussed, together with the charge exchange phenomenon.

3.2.1 Ion beam cooler

As the IGISOL facility is being developed towards applications on rare exotic radioactive beams, the demand for a better beam quality becomes important. A Penning trap, designed for the production of isotopically pure ion beams and for the mass measurements, is currently under construction. Such a device requires a beam of high ion optical quality and, if needed, bunching. Secondly, measurements of collinear laser spectroscopy performed at the IGISOL facility are extremely sensitive on the energy spread of the radioactive beam, which for an IGISOL beam is > 50 eV. Therefore, a cooler device for narrowing the energy spread below 1 eV and providing bunching of the IGISOL beam has been constructed [Niem00].

The cooler is a gas filled radiofrequency quadrupole which cools the 40 keV IGISOL beam. During the cooling process the ions feel a frictional force in He gas and confine themselves on the central axis of the device. The ions are extracted from the gas filled region into the high vacuum region where they are extracted through several extraction elements and further accelerated back to 40 kV voltage.

The cooler has an important role related to the manipulation of ions with q=2+ charge state, which will be of importance in the separation of doubly charged ions in the IGISOL beam. The usefulness of a Wien filter is dependent on the $q=2+ \rightarrow q=1+$ process which takes place in the cooler in carefully defined buffer gas conditions. The charge exchange process was studied both off-line and on-line and the results will be discussed in the next chapter related to the Wien filter.

3.2.2 *Wien Filter*

The operating principle of the velocity filter, introduced by Wien in 1902, is based on mutually perpendicular electric and magnetic fields, E and B. When the two opposing forces are set equal,

$$qvB = qE\,, \tag{3.3}$$

the ions will pass undeflected through the filter. The velocity of these undeflected ions is thus

$$v = \frac{E}{B} \tag{3.4}$$

which is independent on the charge of the ion. However, the velocity of the ions exiting the cooler is given as

$$v = \sqrt{\frac{2qU_{acc}}{m}}\,, \tag{3.5}$$

where U_{acc} is the acceleration voltage of the cooler, and thus the Wien filter in this case eventually separates ions according to their q/m ratio. The principle of the Wien filter is illustrated schematically in Figure 3.4. The magnetic field is produced by a pair magnets, and the perpendicular electric field by a pair of electrostatic deflection plates. The beam, represented by a cross in the middle, is thus effected by the electric and magnetic forces.

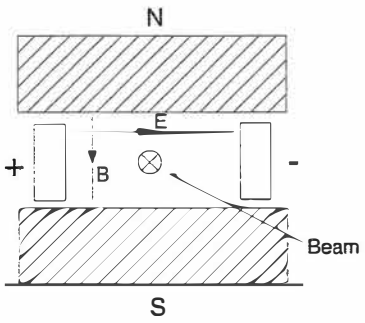

Figure 3.4. Schematic figure of the Wien filter, consisting of a magnet and a pair of electrostatic deflection plates, viewed along the beam direction.

The starting point in the design of the Wien filter was to ensure that the doubly charged ions with mass 140<A<160 are deflected so that they are well separated from the ions with mass 70<A<80. Since the beam exiting from the cooler has a finite size, the deflection of the originally doubly charged ions has to be adequate so that they are fully stopped on a slit following the Wien filter. The length of the available beam line for the Wien filter and the flight path before the slit was about 40 cm, which defined the minimum levels for the electric and magnetic field strengths for adequate deflection. As a conclusion, the proper amount of deflection for a given kinetic energy of the ions was to be established solely by the strengths of the electric and magnetic fields and the effective length of the Wien filter. The design of the Wien filter was realised by using the Poisson Superfish code [Bil98] to calculate the proper magnetic and electric fields with a specific magnet and electrode geometry.

The magnetic field in the Wien filter was created with two Neorem permanent magnets, with a remanence of B_r = 1.12 T and a coercivity of ${}_BH_C$ = 850 kA/m. With a 15 mm gap between the magnets the calculation provided 0.25 T for the maximum magnetic field in the centre of the magnets. By adding an iron yoke around the magnets, the calculation resulted in B=0.66 T, which both shaped and strengthened the field. The calculated magnetic field is shown in Figure 3.5, so that the origin of the axes corresponds to the centre of the Wien filter. The solid lines in the left and the right side of the figure correspond to magnetic fields with an iron yoke perpendicular (transverse) and parallel (longitudinal) to the beam direction, respectively. In addition, the magnetic field without a yoke is shown as a dotted line in the transverse direction and the measured magnetic field in longitudinal direction is shown as circles.

As the magnetic field created by permanent magnets is constant, the parameter to be varied is the electric field. The electric field is created by two parallel copper electrodes, fixed in the gap between the magnets and connected to electric potentials of opposite sign. In order to create a sufficiently wide region of constant electric field in transverse directions (vertical and horizontal) of the beam, the electric potential was divided through 9 narrow strips, connected with resistors. The homogeneity of the electric field in vertical

transverse direction is important so that the ions which are slightly off the symmetry axes in vertical direction would feel the same electric force as the ions travelling in the middle of the symmetry axes. In addition, since the ions are deflected in the horizontal plane, the electric field should be kept constant in a sufficiently wide region in the horizontal direction. In order to achieve such homogeneity for the electric field, the electrodes were connected by strips. Strips of 1 mm width were introduced on two circuit boards at even spacing of 2 mm, which were glued on the surface of the magnets. A 25 mm gap between the electrodes and an applied voltage difference of 5.2 kV, resulted in a electric field value of 2.1 kV/cm in the centre of the filter. This value corresponds to a situation were ions of mass A=80, accelerated by U_{acc}=40 kV, travel through the Wien filter undeflected. The calculated electric field in horizontal transverse direction, is shown in the left of Figure 3.6 (solid line) in comparison with the simulation without the strips (dotted line). The origin of the axes corresponds to the centre of the Wien filter. In vertical direction, the electric field stays constant up to 5 mm off the symmetry axes.

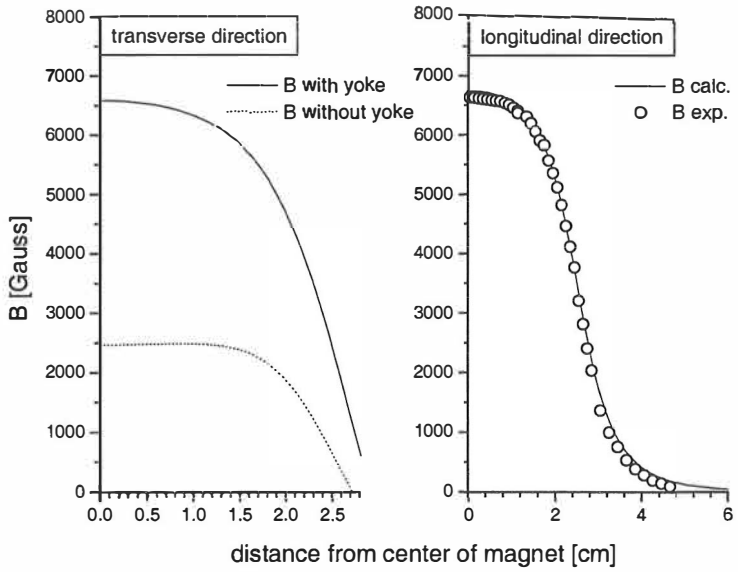

Figure 3.5. Calculated magnetic field perpendicular (solid line on the left) and parallel (solid line on the right) to the beam direction with a magnet gap of 15 mm, including a yoke. The dotted line corresponds to a calculation without a yoke and the circles correspond to measured magnetic field values.

Since the magnetic field is smoothly decreasing towards the edges of the magnets, a similar field shape was designed for the electric field in order to conserve a constant *E/B* ratio both at the entrance and the exit of the filter. The proper shape was attained by setting the electrode length as 40 mm and by introducing slits with a 10 mm aperture at 5 mm distance from the ends of the magnets. The electric field strength along the beam direction, with the described slit configuration, is shown on the right side of Figure 3.6 as a solid line. The magnetic field is illustrated as a dash line, so that the maximum of *B* is normalised to the maximum value of *E*. These two clearly have nearly equal shape. In addition, the calculated electric field without the slit is shown as a dotted line, illustrating the need for a slit.

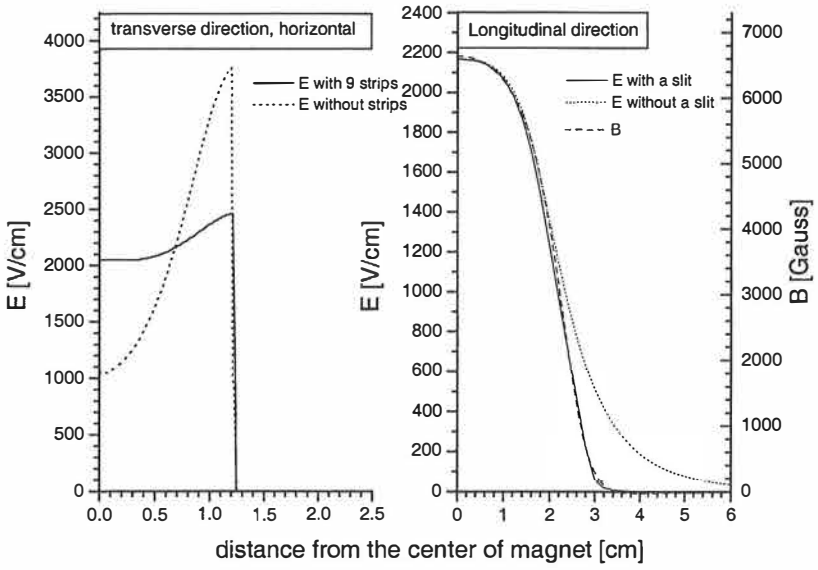

Figure 3.6. Left: Calculated electric field in vertical transverse direction with 9 strips (solid line) and without strips (dotted line). Right: Electric field in longitudinal direction with a slit (solid line) and without a slit (dotted line). As a comparison, the magnetic field is shown as a dash line.

The Wien filter is operated by adjusting the voltage between the electrodes suitable for each undeflected mass and by stopping the deflected ions on a slit at 35 cm distance from the exit. The device, except for the high voltage connectors, is placed inside the vacuum tube, held by adjustable screws for alignment purposes. A technical drawing of the Wien filter is given in Figure 3.7.

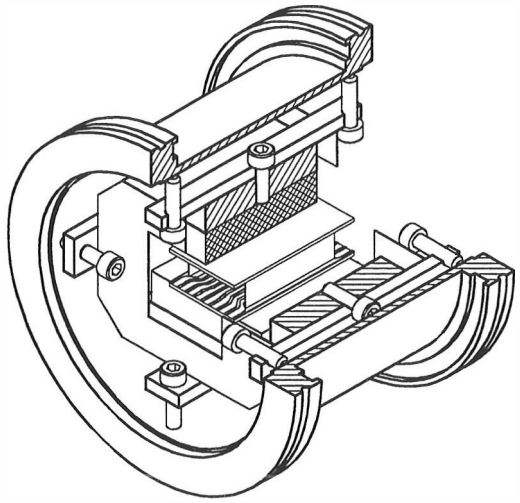

Figure 3.7. Technical drawing of the Wien filter.

3.2.2.1 *Characteristics*

The performance of the Wien filter was tested by using a stable ion beam created by a discharge ion source. A beam of ^{180}Hf ions was extracted from the IGISOL, focused through the cooler and deflected by the Wien filter. The beam current was measured by a Faraday cup after the Wien filter by scanning the electrode voltage difference from 3400 V to 4000 V, illustrated in Figure 3.8. The maximum current corresponds to a voltage difference reading of 3650 V, whereas as the calculated value for an undeflected mass A=180 gives 3420 V. The reason for the difference between the calculated and measured value is that the beam from the quadrupole deflector, after the cooler, is entering the Wien filter slightly off the symmetry axes. Therefore, a slight increase of the electrode voltage is needed to produce the same deflection as was anticipated by the calculations.

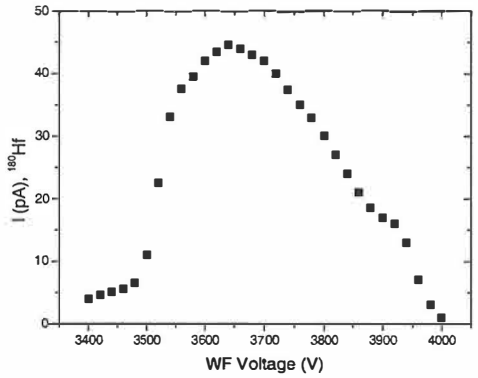

Figure 3.8. Intensity of ^{180}Hf ion beam measured by a Faraday cup after the Wien filter as a function of electrode voltage difference.

The asymmetric shape of the current curve can be explained by an asymmetric shape of the beam exiting the quadrupole deflector after the cooler. The shape of the beam was demonstrated more clearly by measuring the transverse profile of the beam from a slit after the cooler. A single slit was scanned through in horizontal direction from which the current was measured. The derivative of the current gave the actual current profile, which is shown in Figure 3.9. The FWHM of the beam is 2.1 mm and the distance of the two maxima (d=1.5 mm) corresponds to the effect of about 250 V difference in the electrode voltage which was evident in Figure 3.8.

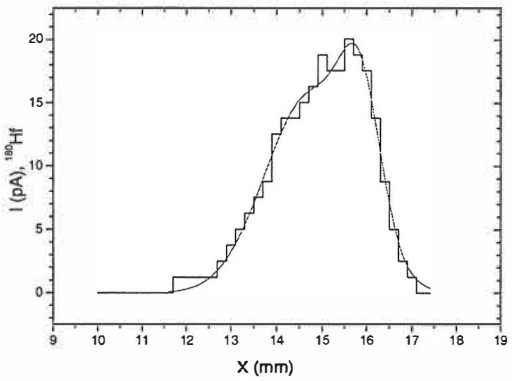

Figure 3.9 Current profile of the ^{180}Hf beam measured on a movable slit after the cooler.

If the width of the beam exiting the Wien filter is 2 mm, which is still an over estimation, the minimum amount of deflection required for the ions to be extracted by a slit is 2 mm. In the mass region A≈70 this corresponds to 7 *m/q* units, which means that the Wien filter can be indeed used to separate the originally doubly charged ions from the singly charged.

3.2.2.2 Charge exchange measurements

The ion cooler plays an essential role related to the proper performance of the Wien filter. The charge exchange process q = 2+ → q = 1+ of the doubly charged reaction products, taking place inside the cooler, is dependent on buffer gas conditions. These are the type of the gas, the total pressure and the amount of impurity molecules in helium. In general, the charge transfer reaction between an ion R with a charge state q+ and a neutral helium atom can be written as

$$R^{q+} + He \rightarrow R^{(q-1)+} + He^{+} + \Delta E, \qquad (3.6)$$

where the energy defect, ΔE, is the difference between ionisation potentials of R and He. Studies concerning the reactions for doubly charged ions at near thermal energies in different gases [Lin83] can be partly adapted to our case in which ions have energy E<1eV after the cooling stage. It turns out that only the exoergicity (ΔE>0), and not the nature of the ion, determines the rate of the electron capture reaction. Therefore, as the first ionisation potential of helium is higher than the second ionisation potential of most of the elements (ΔE<0), then electron capture of a q = 2+ ions in the cooler is energetically very improbable. However, with a proper choice of impurity molecules mixed in helium the electron capture of a q = 2+ ion may become probable. This requires that the first ionisation potential of the impurity molecule is between the first and second ionisation potential of the doubly charged ion. A list of the first and second ionisation potentials of some elements, relative to this work, is given in Table 3.2 .

Table 3.2 1st and 2nd ionisation potentials for several elements [Wea74].

	He	N_2	Cu	Ba	La	Rh
1st ionisation pot. [eV]	24.481	15.576	7.724	5.21	5.61	7.46
2nd ionisation pot. [eV]	54.403		20.29	10.001	11.43	18.07

The charge exchange behaviour of singly charged and doubly charged reaction products was studied on-line with the cooler and the Wien filter. In order to have an idea about the effect of the cooler conditions on different elements, i.e. for ions with different ionisation potentials, two tests were made. In the first test, yields of ^{112}Rh ions, which are strongly produced in proton (E_p=30 MeV) induced fission of ^{238}U, were studied. The q = 1+ and q = 2+ ions were selected separately with the mass separator, according to their dissimilar bending radii, and the choice of the Wien filter voltage enabled to further separate the originally 2+ ions, exiting the cooler either as q = 1+ or q = 2+ ions. The yields of ^{112}Rh ions after the Wien filter were measured for all three cases (q=1+ → q=1+ , q=2+ → q=2+ and q=2+ → q=1+) as a function of nitrogen partial pressure inside the cooler, so that the total pressure was kept constant. The yields are shown in Figure 3.10, so that in all three cases the maximum yield value is normalised as 1. One can see from Figure 3.10 that for the process q = 2+ → q = 1+ there exists a maximum in the yield of ^{112}Rh at a specific nitrogen partial pressure. This can be understood by comparing the ionisation potentials of Rh and N_2 which indicate an endoergicity of the reaction.

A similar examination of the singly charged ^{72}Cu ions, and simultaneously transported doubly charged ^{144}Ba and ^{144}La ions, shows a different kind of behaviour. The yields, obtained from the characteristic radioactive decay of these isotopes, are presented in Figure 3.11 as an intensity ratio of ^{72}Cu/^{144}Ba and ^{72}Cu/^{144}La. In this case only those doubly charged ions which survive from the cooler as q = 2+ are detected, since the q = 1+ ions resulting from q = 2+ → q = 1+ charge exchange reaction are deflected by the Wien filter. The ratio between singly and doubly charged ions in this case does not reach any definite maximum, meaning that the relative amount of doubly charged ions does not

decrease with an increasing partial pressure of nitrogen. This is due to the fact that the electron capture of Ba or La q=2+ ions from a neutral nitrogen molecule is not energetically favourable, since the second ionisation potential of Ba and La is lower than the first ionisation potential of N_2.

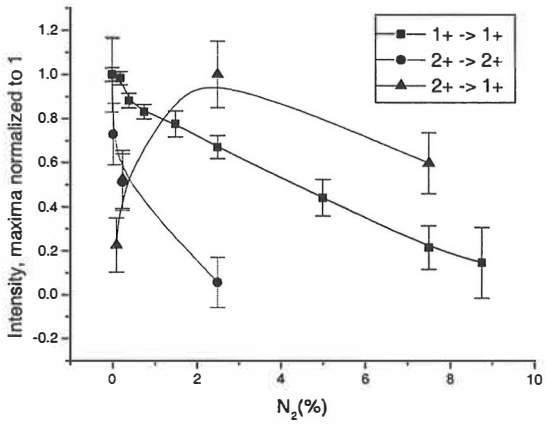

Figure 3.10. Yields of ^{112}Rh as a function of nitrogen partial pressure in the cooler for three different situations of charge transfer: q=1+ → q=1+ (squares), q=2+ → q=2+ (circles) and q=2+ → q=1+ (triangles).

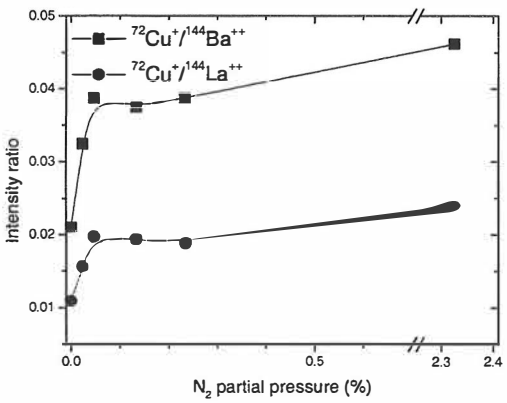

Figure 3.11. Yield ratios of $^{72}Cu^{+}/^{144}Ba^{++}$ and $^{72}Cu^{+}/^{144}La^{++}$ measured after the Wien filter as a function of nitrogen partial pressure in the cooler.

The results obtained with ^{112}Rh give us confidence that with a proper choice of impurity molecules, related to simple ionisation potential considerations, we can control the electron capture process of doubly charged ions in the IGISOL beam. Therefore, in order to enable the lowering of the q = 2+ charge state of Ba and La isotopes, we need to find an impurity gas with a proper first ionisation potential, keeping in mind the various new effects that might arise in introducing chemical compounds in the cooler.

4 Results

The measurements in the present work were done partly at the ISOLDE mass separator facility at CERN and partly at the accelerator laboratory of the University of Jyväskylä. Two experiments were performed at ISOLDE, concentrating first on the β decay of $^{34-35}$Al and later, as a continuation, the β decay of ^{33}Na. The later experiment included also a lifetime measurement in connection to the first experiment concerning the level structure of ^{35}Si. The results of the β decay study of all these three nuclei will be discussed separately in the following text. The experiment which took place in Jyväskylä concentrated on superasymmetric fission yields. The results will be presented in the end.

4.1 Beta decay of ^{34}Al

The β decay of ^{34}Al serves as a source of information on the level structure of its daughter nucleus, ^{34}Si. The first experimental results for the β decay of ^{34}Al were obtained at GANIL by a fragmentation reaction [Duf86], yet not revealing the level structure of ^{34}Si. Three years later at the ISOLDE facility results on the ^{34}Al β decay to bound levels in ^{34}Si were obtained [Bau89]. These results will serve as a starting point for our present work. The improvement in the production yield of ^{34}Al, compared to the previous measurement, corresponds to a factor of three, thus allowing a higher statistics for the analysis. Our half-life analysis was based on two methods, namely on characteristic γ lines following the β decay of ^{34}Al and β multiscaling. The former gives a value of $T_{1/2}$=55.6(1.3) ms and the latter $T_{1/2}$=56.4(6) ms, resulting in a weighted average of $T_{1/2}$=56.3(5) ms. The decay of the strongest γ lines, and a fit for the half-life, is represented in Figure 4.1. As a comparison, the previous reported value for the ^{34}Al half-life was 42(6) ms [Ree95].

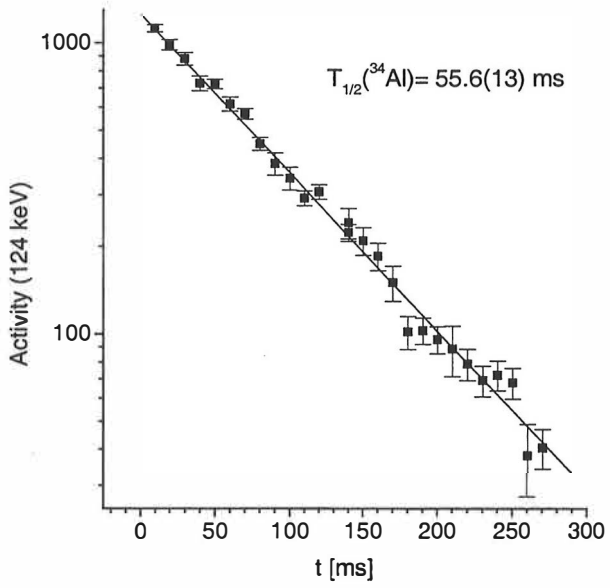

Figure 4.1. Decay-time spectrum of the 124 keV line associated with the β decay of ^{34}Al. The reported half-life value for ^{34}Al is 56.3(5) ms, which is obtained by the weighted average of 55.6(13) ms from the 124 keV transition, and 56.4(6) ms from β multiscaling.

The level scheme of ^{34}Si was investigated by a γ–γ coincidence analysis as well as by a half-life analysis. The latter provided means to associate γ transitions to their proper β decay. The previously reported four γ transitions (124, 929, 3326 and 4255 keV) are confirmed, as well as the three reported excited states with their spins and parities. In addition, four new γ transitions (591, 1010, 1053, 1435) were assigned to the β decay of ^{34}Al and placed in to the decay scheme. A singles γ spectrum of A=34 is shown in Figure 4.2 where the strongest lines belonging to the ^{34}Al β decay are indicated, together with the contaminants. The transitions and their intensities are listed in Table 4.1.

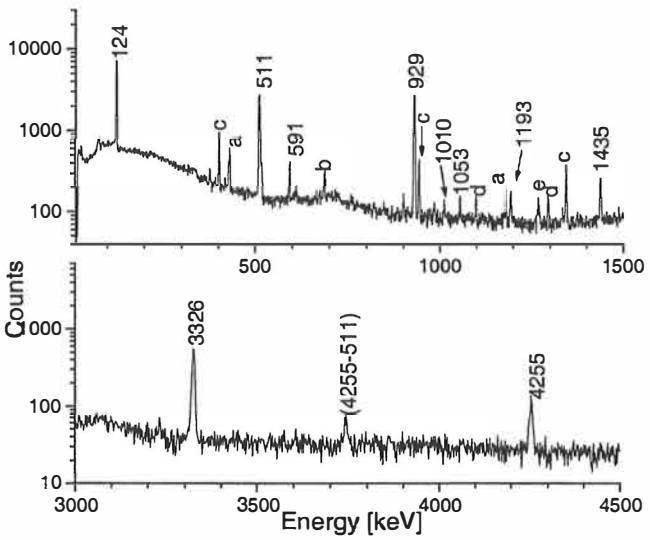

Figure 4.2. Partial γ spectra taken in coincidence with β particles at A=34. Peaks identified by their energy in keV are from ^{34}Al β decay. Those labelled by a letter are from the decay of (a) ^{34}Si, (b) ^{204}At (6+ in A=34), (c) ^{28}Mg, (d) ^{116}In (4+ in A=29) and (e) ^{29}Al.

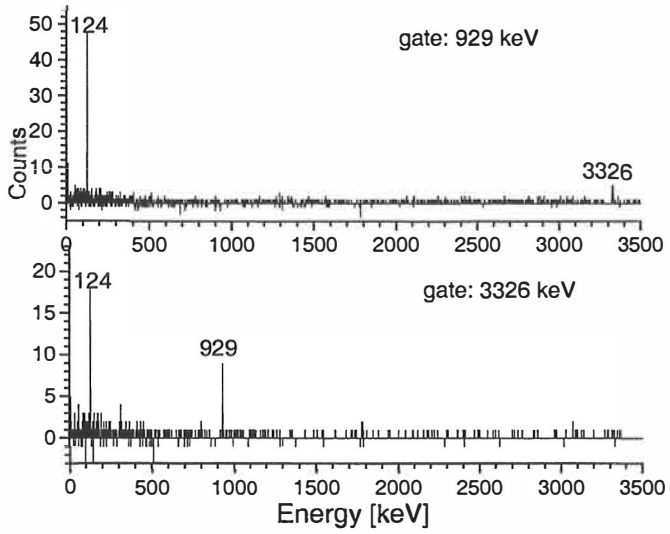

Figure 4.3. β-gated γ–γ spectra at A=34. Coincidences with 929 keV (upper) and 3326 keV (lower part) γ rays.

Table 4.1. Energy and intensity of γ rays attributed to the ^{34}Al decay.

Energy (keV)	Intensity[a] (relative)	Transition	
		From	To
124.21 (40)	51.9 (4.3)	4379	4255
590.85 (30)	7.7 (0.8)	4970	4379
928.98 (30)	103.9 (9.7)	4255	3326
1009.69 (40)	2.7 (0.4)	b	
1052.76 (40)	3.9 (0.6)	4379	3326
1193.34 (29)	6.4 (0.8)	c	
1434.86 (50)	13.9 (1.4)	b	
1715.42 (80)	2.4 (0.4)	d	
2696.43 (1.2)	4.8 (1.0)	d	
3326.24 (1.6)	100	3326	0
4257 (3)	24.0 (3.8)	4255	0

[a] Intensities are relative to the 3326 keV γ-ray. The intensity per 100 β decays is obtained by multiplying by a factor 0.55
[b] Corresponding to a transition in the ^{33}Si level scheme following neutron emission
[c] See the discussion
[d] Unplaced in the decay scheme

The 591 keV γ transition is found in coincidence with the 124 keV transition. However, it is not observed in coincidence with any other transition, which is explained by the high detection efficiency of 124 keV compared to the other transitions in ^{34}Si. As an example, two coincidence spectra are shown in Figure 4.3 which clearly demonstrate the γ-ray sequence of 124 keV, 929 keV and 3326 keV. The 159 keV transition is placed above the 4379 keV level as no other interpretations seems likely. Another new transition, with 1053 keV energy, is placed in the level scheme due to the energy difference of the known 4379 keV and 3326 keV levels.

The remaining two new γ transitions do not appear to be in connection with the level scheme of ^{34}Si. In fact, they are assigned to follow the β-delayed neutron emission of ^{34}Al. For the 1435 keV transition we find three experimental arguments supporting this interpretation. First, the 1435 keV transition is found in coincidence with neutrons. Secondly, this transition is not observed in coincidence with high energy β's, referring that the final state of the β decay is above the neutron separation energy of ^{34}Si (S_n=7.54 MeV) enabling a neutron emission to occur. Thirdly, a γ transition with equal energy has been reported in heavy-ion induced reaction studies which investigated the ^{33}Si level scheme [For94, Fif85]. In these works, the γ transition was attributed to the 1435 → 0 keV transition and $J^\pi = 7/2^-$ has been proposed for the 1435 keV level. Knowing that the final state of the β decay of ^{34}Al ($J^\pi = 4^-$) in ^{34}Si is likely to have spin and parity of $J^\pi = 3^-$,4^-,5^-, it is indeed very likely that with an l=0 neutron emission the final state in ^{33}Si is $7/2^-$, which is deexcited by the 1435 keV γ transition.

Finally, for the 1010 keV transition there are no experimental arguments related to β delayed neutron emission but only support from the literature. A state at 1010 keV energy in ^{33}Si has been reported in deep-inelastic reaction studies [For94] and similarly a state at 1060(20) keV [Fif85] and 1040(29) keV [May84] has been reported in heavy ion transfer reaction studies. So far there is no experimental spin and parity assignment for the level but shell model calculations indicate $J^\pi = 1/2^+$ assignment for the first excited state in ^{33}Si. Applying a similar reasoning as for the 1435 keV level we can see that the 1010 keV level cannot be populated directly in the β-delayed neutron emission. Instead, it will be most probably populated by γ transitions from higher excited $J^\pi = 3/2^+,5/2^+$ states in ^{33}Si which are the final states of angular momentum l=1 neutron emission of $(3,4)^-$ states in ^{34}Si, populated by GT transitions.

In such cases where the β-delayed neutron emission is an alternative decay mode to β decay we have to determine the probability, P_n, for neutron emission. This factor has to be then taken into account in determining the β decay log *ft* values and β branchings. Experimentally, the P_n value is determined by comparing the activity corresponding to

direct β decay with the activity from β delayed neutron emission. In the case of ^{34}Al, we observed γ rays belonging to the ^{33}Si β decay, which is a clear indication of the β delayed neutron emission. However, we do not know the amount of β-delayed neutron emission which decays directly to the ground state of ^{33}Si. Therefore, the P_n value has to be determined one generation downwards, from the γ transitions following the β decay of ^{33}Si to ^{33}P. This decay scheme is well known and we only have to assume that the β branch from ^{33}Si ($J^{\pi} = 3/2^{+}$)to the ^{33}P ground state is negligible [Wil83]. The total activity of direct β decay of ^{34}Al was determined from the 930 keV transition in ^{34}Si and the β-delayed neutron activity was determined from the 1847 keV transition in ^{33}P, both corrected with their proper absolute intensities. Furthermore, an additional correction had to be made to the activity of ^{33}Si because the collection tape was moving the activity away after every tenth proton pulse. Therefore, the relatively long half-life of ^{33}Si, $T_{1/2}$=6.18 s, appears as a loss of activity. This correction was done by simulating simultaneously the direct production of ^{34}Al in ISOLDE conditions, with the same beam gate settings as in the experiment, and the production of ^{33}Si only through β decay of ^{34}Al with a 100% branch. This yielded a correction factor of 0.35(3) which represents the observed amount of ^{33}Si in a time interval of 0.01-0.9 s (experimental condition) compared to the total produced amount. With this correction we obtained P_n = 26(4)% which is in good agreement with the previous reported value by Baumann *et al.* (27(5)%) [Bau89]. The discrepancy with previously measured values by Bazin *et al.* (54(12)%) [Baz88] and Reeder *et al.* (12.5(25)%) [Ree95], however, is large. We did not observe any γ transition belonging to the ^{32}Si decay scheme, and therefore conclude that there occurs no β-delayed two-neutron emission.

We could say that our most important goal in improving the knowledge of the level structure of ^{34}Si was to find the first excited 0^+ (0^+_2) state predicted by shell model calculations. The shell model predicts that the branching ratio for the $2^+_1 \rightarrow 0^+_2$ transition is very small, only few percent, which is a direct consequence from the energy difference between the $2^+_1 \rightarrow 0^+_2$ and $2^+_1 \rightarrow 0^+_1$(g.s.) transitions. This makes our experimental situation fairly difficult. By examining our statistics in γ–γ coincidences we realise that it

is nearly impossible to observe this $2^+_1 \rightarrow 0^+_2$ transition in coincidence with any upper γ transition with our present statistics. Therefore, we can use only the γ-singles spectra for the search of this transition and have to rely on shell model predictions and measured *B(E2)* values. From the singles spectra we find only two γ transitions, besides the ones already mentioned earlier, which fulfil the half-life condition of ^{34}Al, that is 1193 keV and 1715 keV. The corresponding 0^+_2 level in ^{34}Si would thereby be either at 2133 keV or 1611 keV.

Before going into details on the *B(E2)* analysis we have to make a correction for the intensities of the γ transition candidates $2^+_1 \rightarrow 0^+_2$ compared to the intensity list in Table 4.1. We will now examine the 1193 keV case. If the γ transition is not associated with the $2^+_1 \rightarrow 0^+_2$ transition, it will be detected in similar conditions as the 3326 keV transition and the intensity for the 1193 keV transition is 6.4(8)%. However, if the 1193 keV transition corresponds to the $2^+_1 \rightarrow 0^+_2$ transition, the final state is the 0^+_2 state, which will decay to the ground state either by 2γ-emission, e^+e^- pair emission or by atomic electron emission. The most probable decay mode in this case is the e^+e^- pair emission, for which we denote a probability P_π. From Wilkinson *et al.* [Wil69] we can calculate that $P_\pi/P_e = 49$, P_e being the probability of atomic electron emission. The probability for 2γ emission, $P_{\gamma\gamma}$, is expected to be very low. The pair emission will have an effect on the experimental trigger condition, so that the detection of 1194 keV γ rays can be triggered by the β as well as by any of the two electrons emitted in the decay. Therefore, we have to calculate what is the probability of detecting at least one of these three events, i.e. the real trigger. If we call the β-detection probability for a single event P, the probability for the trigger is $1-(1-P)^3 = 3P(1-P)+P^3$. In our experiment this results in a factor of 2.00(25) for the increase of the detection efficiency associated with a pair emission. The relative intensity of the 1193 keV transition should be in this case 3.2(6), whereas in Table 4.1 it is 6.4(8). The modified intensity will be used in the *B(E2)* analysis described in the Discussion chapter.

The revised decay scheme is shown in Figure 4.4. The Q_β value has been taken from ref. [Aud97]. As it was stated in the very beginning of this chapter, we corroborate the previously reported levels energies, as well as spin and parity assignments. In ref. [Bau89] the excited state at 3326 keV has been assigned as $J^\pi = 2^+$ according to the γ decay mode and the absence of β feeding. In addition, Coulomb excitation measurements [Ibb98] confirm this assignment. Two states, at 4255 kev and 4379 keV, are strongly fed by β decay of the ^{34}Al negative-parity ground state. Therefore, negative parities are deduced for these two states from their allowed character. The assignment for the 4255 keV state is based on two facts. First, we know from shell model calculations [War88] that the ground state of ^{34}Al is either 3^- or 4^-. Secondly, the timing properties of the 4255 keV level indicate an E3 character for the 4255 keV γ transition, resulting in only one possible value, $J^\pi = 3^-$, for this state. Consequently, for the ground state of ^{34}Al, $J^\pi = 4^-$ is established. The states at 4379 keV, as well as at 4970 keV, result from allowed decay and therefore the spin and parity assignment for both is either 3^-, 4^- or 5^-. The new log *ft* values, β branchings and spin and parity assignments are given in Table 4.2.

Table 4.2. β intensities and log ft values in the ^{34}Al β decay to bound levels in ^{34}Si.

E_x (keV)	I_β(%)	log *ft*	J^π
0			0^+
2133.1 (5)	< 1	> 6.8	(0^+)
3326.4 (3)	< 12	> 5.5	2^+
4255.4 (5)	44 (4)	4.90 (6)	3^-
4379.5 (5)	26 (3)	4.90 (5)	$(3,4,5)^-$
4970.4 (7)	4.2 (4)	5.70 (7)	$(3,4,5)^-$

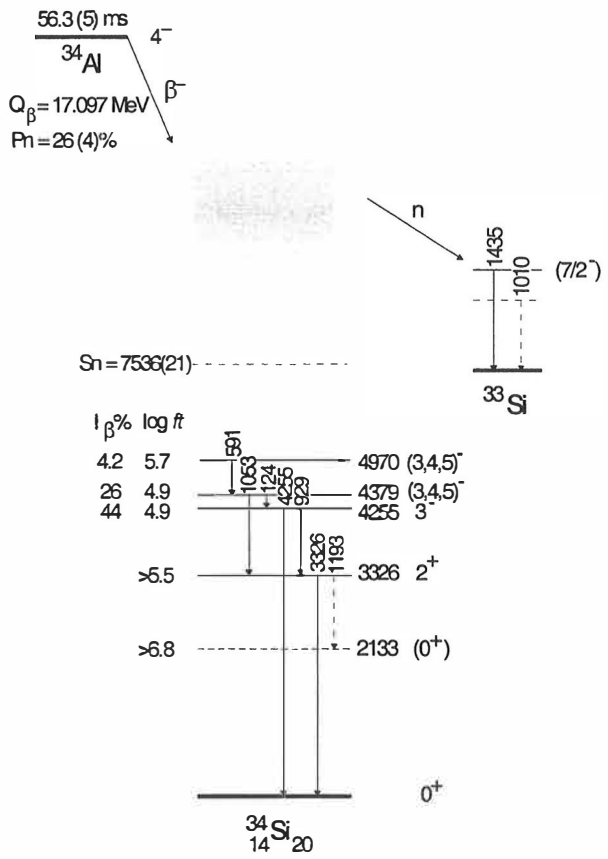

Figure 4.4. ^{34}Al β-decay scheme

4.2 Beta decay of ^{35}Al

It was already anticipated by numerous calculations that the level scheme of ^{35}Si, yet unknown, would reveal important features about the shell structure around the island of inversion. The level energies and spin and parity assignments would fix the single neutron excitations in a clear manner, introducing important data points for shell model parameters. Previous experiments on the β decay of ^{35}Al reported half-life values of $T_{1/2}$= 150(50) ms [Lew89] and later $T_{1/2}$= 30(4) ms [Ree95]. Yet, no γ transitions were reported

belonging to this decay. In our experiment we were able to observe β decay branches of ^{35}Al and to build the first level scheme of ^{35}Si.

As in the case of ^{34}Al, the half-life of ^{35}Al β decay was measured both from the β counting and the decay of the strongest γ transitions. The decay spectrum of the two strongest γ transitions, 64 keV and 910 keV, is shown in Figure 4.5. Taking the average of the independent β and γ measurements, we obtain the weighted mean value of 38.6(4) ms.

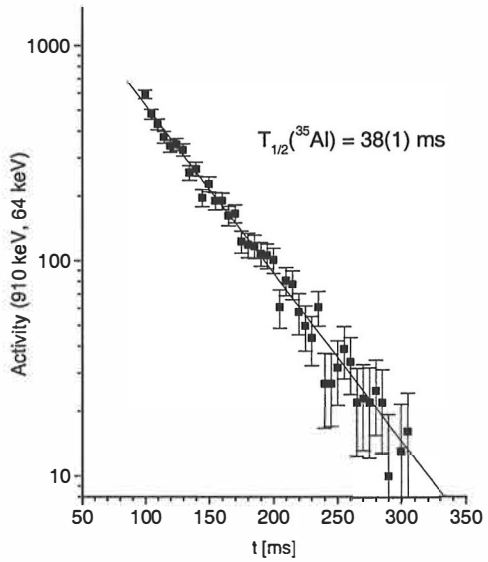

Figure 4.5. Decay-time spectrum of the 64 and 910 keV lines. The result of the fit, which is indicated, has been combined with independent β measurements to get the adopted value of the ^{35}Al half-life $T_{1/2}$ = 38.6(4) ms.

In the mass separated beam of A=35, we observed altogether 10 γ transitions which clearly exhibited a half-life behaviour related to β decay of ^{35}Al. In Figure 4.6 three γ spectra are shown. The middle one corresponds to a time window of the first 300 ms after the proton pulse, and the lower figure shows the following 300 ms. Since the ISOLDE beam was on only for 100 ms, γ transitions from the short-lived ^{35}Al will appear only in the first window. The two strongest γ lines are clearly in coincidence, which can be seen

in the coincidence spectrum of 64 keV in the upper part of Figure 4.6. A γ transition, with energy of 974 keV, corresponds to a cross-over transition of the cascade 64 - 910 keV and the 2168 keV is attributed to a branch to the ground state of ^{35}Si from a level at this energy. Out of the remaining transitions still one, with 1194 keV energy, is placed in the level scheme of ^{35}Si according to the energy difference between the 2168 and the 974 keV levels. It should be noted, that this line differs in energy from the line we reported in the A=34 study, namely 1193.3(2) keV. The list of the γ transitions assigned to the ^{35}Al β decay, together with their intensity, is given in Table 4.3. In each transition there is an indication whether it belongs to the level scheme of ^{35}Si or whether they correspond to transitions in the ^{34}Si level scheme following β-delayed neutron emission. Only one γ ray remains unplaced.

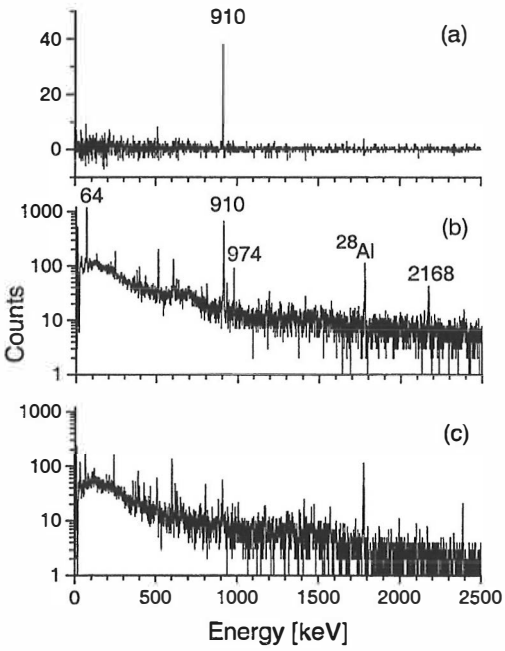

Figure 4.6. Partial γ spectra taken in coincidence with β particles at A=35. In the upper part (a), the γ spectrum in coincidence with β detection gated by the 64 keV line. In (b) and (c), the γ spectrum in coincidence with β detection and registered in two time bins: 0-300 and 301-600 ms, respectively, after collection. All peaks in the spectrum have been identified and belong to daughter activities or long half-life contaminants.

Table 4.3. Energy and intensity of γ rays attributed to the ^{35}Al decay.

Energy (keV)	Intensity[a] (relative)	Transition	
		From	To
64.05(30)	100	974	910
124.20(30)	2.5(1.9)	b	
910.11(30)	99.7(1.9)	910	0
929.12(40)	5.8(1.3)	b	
973.78(20)	11.8(2.4)	974	0
1130.28(40)	3.2(0.9)	c	
1194.20(40)	5.3(1.2)	2168	974
2168.24(60)	15.2(3.1)	2168	0
3326.96(70)	18.0(3.6)	b	
5629(3)	2.4(1.2)	c	

[a] Intensities are relative to the 64 keV γ-ray. The intensity per 100 β decays is obtained by multiplying by a factor 0.45
[b] Corresponding to a transition in the ^{34}Si level scheme following neutron emission
[c] Unplaced in the decay scheme

The β-delayed neutron emission probability was obtained by measuring relative daughter activities, both from direct β decay and β-delayed neutron emission. The activities of direct β decay and β delayed neutron emission were obtained from the 1572 keV and 2129 keV γ rays, belonging to the β decay of ^{35}P and ^{34}P, respectively. The collection tape was not moving, hence no correction for the activity was needed. The result is P_n = 41(13)% which is considerably larger than the previously reported value, P_n = 26(4)% [Ree95]. However, the agreement with en earlier ref. [Lew89], is very good. We did not find any evidence for A=33 activity, which means that the amount of 2n emission is negligible.

In practice, the only way to probe levels above the neutron separation energy ($S_n(^{35}Al)$ = 2474(43)) is to measure the energy of β-delayed neutrons, which in this work was carried out with time-of-flight technique. The delayed neutron spectrum for A=35 is shown in Figure 4.7, together with the ^{29}Na spectrum, used for detection efficiency control. The spectrum is dominated by a prompt β-γ coincidence, which in Figure 4.7 is marked off from the left. Among the real neutron events one can observe two maxima around 3.0 MeV and 0.98 MeV. Since it is more probable that the delayed neutrons, with angular momemtum l=0, feed the excited 2^+ state (3326 keV) in ^{34}Si than the 0^+ ground state, we can trace up the excited levels in ^{35}Si involved in this process approximately up to 8.9 MeV.

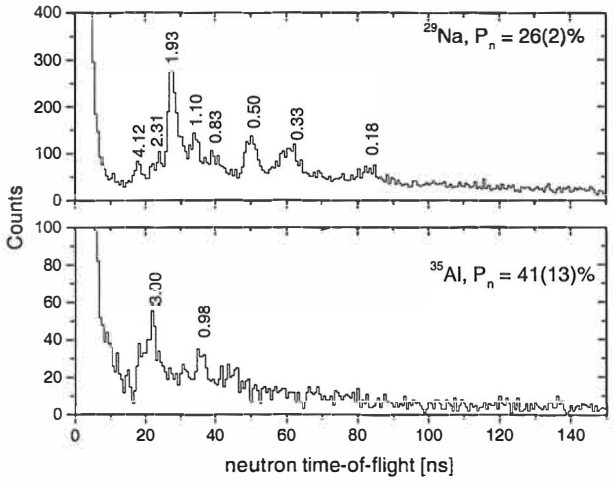

Figure 4.7. Neutron time-of-flight spectra taken under identical conditions with the ^{29}Na sources (upper part) and with the ^{35}Al nuclei (lower part). The time scale is 78 ps/channel. Neutron energies are labelled in MeV.

Before stating the β branches for the excited states in ^{35}Si, we should evaluate the ground state branch. First, we can assume that there is no direct production of ^{35}Si. By measuring the total γ intensity from the decay of excited states of ^{35}Si and comparing it with the decay of ^{35}Si, we can deduce a ground state branch of 3(1) %. This corresponds to a first

forbidden decay, which has already been foreseen by theory. Putting together the results for the ground state branch and the P_n value, together with a Q_β value [Aud97], we can calculate the log *ft* values and β branchings, listed in Table 4.4. The conversion coefficient of the 64 keV transition is only 0.04 and therefore it can be neglected.

Table 4.4. β intensities and log ft values in the ^{35}Al β decay to bound levels in ^{35}Si.

E_x (keV)	I_β(%)	log ft	J^π
0	3.0(10)	6.04(14)	$(7/2)^-$
910.10(30)	<0.9	>5.15	$(3/2)^-$
973.80(30)	48(9)	4.70(8)	$(3/2)^+$
2168.10(60)	9.2(19)	5.22(9)	$(5/2)^+$

From the obtained log *ft* values we learn about the spin and parity assignment for the ground state and first three excited states. For the ^{35}Al ground state we have adopted as $J^\pi = (5/2)^+$ from the systematics in Al isotopes. The shell model calculations predict that the first positive parity state in ^{35}Si results from a 1p-1h configuration with a $d_{3/2}$ neutron hole. According to the log *ft* values the β branch to the 974 keV level is clearly an allowed GT decay, and therefore we can propose a $J^\pi = (3/2)^+$ assignment for this level. For the ground state we propose a $J^\pi = (7/2)^-$ assignment, corresponding to a $f_{7/2}$ neutron. This interpretation is supported by previous calculations [Woo86, War87] and also by the systematic trends in neighbouring nuclei [Aud95]. The first excited state, which also has a first forbidden character, is proposed as $J^\pi = (3/2)^-$ corresponding to a $p_{3/2}$ neutron. This is expected from the N=21 isotone systematics. The energy of this level, however, is defined by the order of the 64 keV and 910 keV γ transitions.

The order of the 64 keV and 910 keV transitions cannot be deduced from their intensities since there is only β feeding from above and the transition intensities are equal within error limits. Therefore, the order should be deduced from level-lifetime considerations.

We already stated the spin and parity assignments for the 3 lowest states, namely $(7/2)^-$, $(3/2)^-$ and $(3/2)^+$. Hence, the lower transition implies a quadrupole character ($3/2^- \rightarrow 7/2^-$). If the 64 keV transition would correspond to this E2 transition, the lifetime would be in the microsecond range. Instead, such a lifetime was not observed. This serves as a strong argument that the 64 keV is above the 910 keV transition.

A more detailed lifetime analysis, concerning the 64-910 keV cascade, was performed in a separate experiment. The lifetime of the $J^\pi = (3/2)^+$ level was deduced by measuring coincidences between a thin plastic detector (β) and a BaF2 scintillator (γ). We observed that the 64 keV line as well as the 910 and 974 keV lines gave delayed events on the time spectra and a careful analysis leads to a lifetime value of $\tau = 8.5(9)$ ns for the 974 keV level. Branching ratios of the 64 keV and 974 transitions lead to partial widths, which again can be expressed in Weisskopf units, yielding $\Gamma/\Gamma_W = 0.35(4) \cdot 10^{-3}$ for the 64 keV E1 transition and $\Gamma/\Gamma_W = 0.061(7)$ for the 974 keV M2 transition. These values are typical for similar transitions in light nuclei [End93].

Based on the above-mentioned observations and results we propose a decay scheme for ^{35}Al in Figure 4.8. The spin assignments for the 3 lowest levels are kept in parenthesis, mainly because the spin on the ^{35}Al ground state is not yet well established experimentally. The parities, though, can be stated with certainty. Finally, the spin value of the 2168 level can be limited to $J^\pi = (3/2 - 7/2)^+$ according to log *ft* considerations. The relative intensities of the two decay branches of the 2168 keV level are compatible with E1 and M1 radiations for the 2169 keV and 1194 keV transitions, respectively, which can narrow the assignment as $(5/2)^+$. Moreover, a comparison with *B(GT)* calculations, presented in the discussion chapter, is in favour of this assignment.

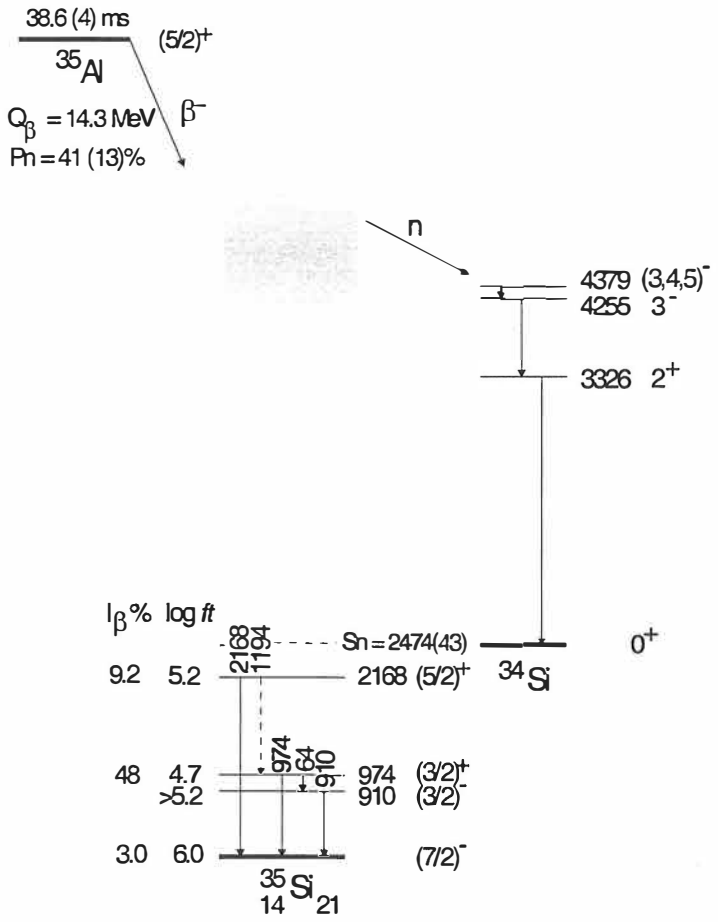

Figure 4.8. ^{35}Al β-decay scheme

4.3 Beta decay of ^{33}Na

The β decay of ^{33}Na was observed already more than 15 years ago [Gui84, Lan84], however, no information on the decay scheme was obtained apart from 6 unplaced γ transitions [Gui84]. Partly due to increased production yields, we were now able to observe altogether 19 γ transitions, some of which could be found in γ–γ coincidences. The γ transitions were identified according to the known half-life of ^{33}Na ($T_{1/2}$=8.2(4) ms)

[Gui84], which provides an unambiguous method to determine the origin of the transitions. The half-life of ^{33}Na can be evaluated according to the decay of the strongest γ transition, 885 keV, which resulted in $T_{1/2}$=8.1(4) ms. This is in excellent agreement with the previously reported value by Guillemaud *et al.*. The decay curve for the 885 keV transition is shown in Figure 4.9.

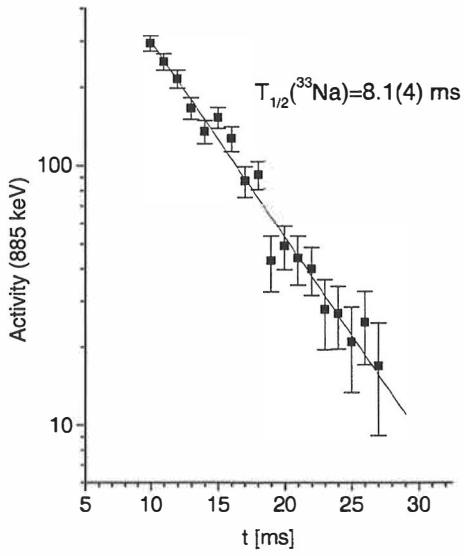

Figure 4.9. Decay-time spectrum of the 885 keV line.

The half-life of ^{33}Na could be as well determined from gross β activity by unfolding the various existing β activities in the continuous β spectrum. The β activity analysis results in $T_{1/2}$=7.9(4) ms and the procedure of the analysis is described in ref. [Rad01]. Similarly, the third corresponding method for half-life determination is through β-delayed neutron activity. In this case the number of parameters is less compared to the β activity method, since there are only few daughters in the ^{33}Na decay chain with a considerable neutron emission probability (^{33}Mg, ^{32}Mg, ^{31}Mg). The sources of inaccuracy are the errors in daughter half-lives and the limited statistics due to low total neutron efficiency. The analysis resulted in $T_{1/2}$=8.0(7) ms [Rad01]. As a conclusion, all three independent methods for half-life determination of ^{33}Na result in $T_{1/2}$= 8.0(3) ms.

The γ spectrum for A=33 is shown in Figure 4.10. The upper spectrum corresponds to a time window up to 50 ms after the arriving proton pulse (a) and the lower corresponds to the following 50-500 ms (b). There are 19 γ lines, which are only visible in the upper spectrum and we assign these to the β decay of ^{33}Na on the basis of their decay rate. The transitions are listed in Table 4.5 together with their absolute intensities and observed coincidences. Lines corresponding to multiple charged contaminants (e.g. ^{198}Bi) are also indicated in the spectra, as well as transitions corresponding to the β decay of ^{33}Si ($T_{1/2}$=6.18 s) and ^{32}Mg ($T_{1/2}$=96(16) ms).

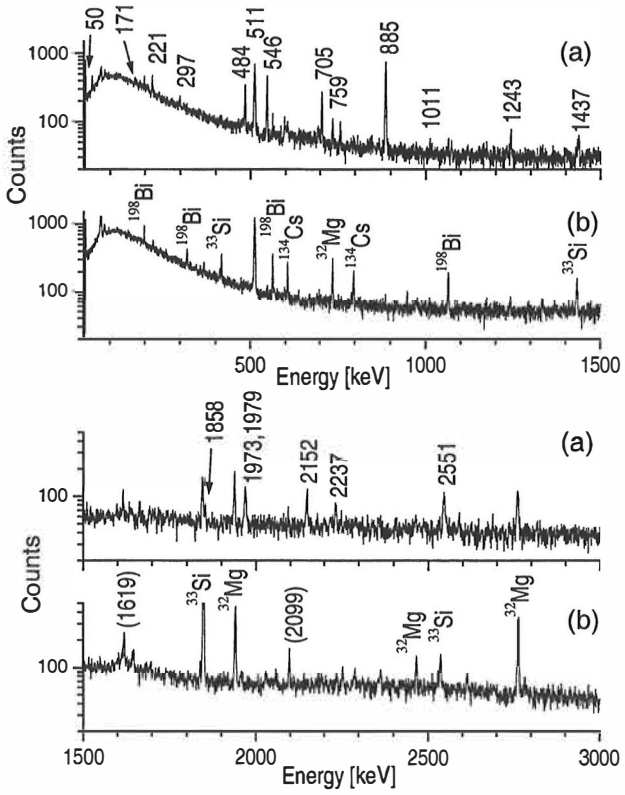

Figure 4.10. γ spectra taken in coincidence with β particles at A=33. The spectrum (a) is registered in time bins 0-50 ms, and spectrum (b) in time bins 50-500 ms, with respect to the proton pulse.

Table 4.5 Energy and intensity of γ-rays attributed to the ^{33}Na decay.

Energy (keV)	Intensity[a]	Transition		Coincidences
		From	To	
50.5(2)	8.2 (9)	c		
171.2(1)	3.5 (4)	c		
221.0(1)	8.7 (10)	705	484	484
	1.4 (2)	c		
	d			
297.9(1)	4.0 (4)			
484.1 (1)	18.7 (19)	484	0	758
546.2 (1)	40.2 (41)	(705)	(159)	
704.9 (1)	23.2 (21)	705	0	
758.5 (1)	6.1 (7)	1243	484	
845.7 (2)	2.5 (4)			
885.3 (1)	100.0	b		
1011.3 (2)	1.6 (4)			
1242.8 (2)	7.1 (10)	1243	0	
1437.0 (3)	4.7 (8)	b		
1857.7 (4)	4.1 (6)			
1972.9 (5)	5.9 (10)	b		
1976.9 (5)	6.7 (10)			
2152.4 (1)	10.3 (21)	b		885
2236.9 (5)	7.0 (9)			
2551	16.0 (17)	b		

[a] Intensities are relative to the 885 keV γ ray. The intensity per 100 β decays is obtained by multiplying by a factor 0.22(8)
[b] corresponding to transition in the ^{32}Mg level scheme following 1n-emission
[c] corresponding to transition in the ^{31}Mg level scheme following 2n-emission
[d] γ line observed in the second time window (50-500 ms), corresponding to a transition in the ^{32}Al level scheme, following 1n emission.

Due to the large Q_β window (20.3(15) MeV [Aud97]) in ^{33}Na β decay, the probabilities for β-delayed one- and two-neutron emission are large. Therefore, γ transitions belonging to the level schemes of ^{31}Mg and ^{32}Mg can be observed. Five γ transitions are associated to the β-delayed one-neutron emission of ^{33}Na, according to the known level scheme of ^{32}Mg [Det79, Det83, Gui84, Klo93]. Out of these, the 885 keV γ transition is the most intense one, corresponding to the $2^+_1 \rightarrow 0^+_1$ transition in ^{32}Mg. This transition was also observed in coincidence with neutrons. Three γ transitions can be identified according to the ^{31}Mg level scheme [Klo93], and therefore they can be associated to the β-delayed two-neutron emission. All of them were also recognised in the neutron coincident γ spectrum. The 221 keV line, which is partly interpreted by a transition in ^{31}Mg, was also observed in coincidence with 484 keV and 735 keV transitions, and therefore can be assigned to the level scheme of ^{33}Mg. Furthermore, a transition with similar energy is also related to the ^{32}Al level scheme [For97]. In Table 4.5, the intensity of the 221 keV γ transitions is divided between the first two contributions (^{33}Mg and ^{32}Mg), whereas the contribution of ^{32}Al was only observed in the second time window (50-500 ms) of the γ spectrum.

We are left with 10 γ transitions out of which the level scheme of ^{33}Mg should be built. In fact, six of them can be placed in the level scheme according to γ–γ coincidence data or according to the sum of γ ray energies. The 484 keV and 221 keV transitions are observed in coincidence. Also, a γ transition of 705 keV energy, corresponding to the sum of (484+221) keV, is observed. The 484 keV and 759 keV transitions are also found in coincidence. The sum of these two transitions, 1243 keV, corresponds to a line in the γ spectrum.

The 546 keV line, which is the second strongest line in the γ ray spectrum, is not found in coincidence with any other γ ray. Therefore, we have different alternatives for its origin. First, it could originate from β-delayed one neutron emission, thus belonging to the level scheme of ^{32}Mg. However, this hypothesis seems highly unlikely in an even-even

nucleus, since such a strong transition either below or above the first 2^+ state would have been revealed in previous studies [Ibb98, Klo93]. Secondly, the 546 keV line is not observed in coincidence with neutrons, whereas the 885 keV line clearly was. Therefore, the 546 keV transition should be located in the ^{33}Mg level scheme, either decaying from a postulated level at 546 keV or, alternatively, decaying from some energetically higher level established through γ–γ coincidences. These two cases will be discussed later.

The absolute γ intensities were evaluated according to a well-known β emitter, ^{26}Na. The γ and β activity of this nucleus was measured with the same set-up and in the same experiment as ^{33}Na, and with a procedure described in ref. [Bau98], resulting in the ratio of β and γ efficiencies, $\varepsilon_\gamma/\varepsilon_\beta$. Similarly, the γ energy spectrum of ^{33}Na was recorded together with the β multiscaling spectrum, so that the contribution of ^{33}Na was extracted from the competing activities. By applying $\varepsilon_\gamma/\varepsilon_\beta$ to the number of simultaneously observed β's and γ lines of ^{33}Na decay, the absolute γ intensities for 100 β decays were deduced.

Concerning the P_n determination for ^{33}Na, the case is now somewhat more complicated than what it was for ^{34}Al and ^{35}Al decays. Since the β decay schemes of ^{33}Mg and ^{33}Al are not yet well established, and because the direct production of ^{33}Al was not negligible, the P_n value cannot be determined directly from γ intensity analysis. However, an upper limit for the P_n value could be determined by comparing the γ transition intensities in the direct β-decay channel (^{33}Mg) and in the β-delayed neutron branch (^{32}Al; 1941 keV and ^{31}Mg, 947 keV). This resulted in P_n ($P_n=P_{1n}+2P_{2n}$) less than 86%. A more precise analysis for determining the P_n value was based on observing β-delayed neutrons so that the total neutron activity was compared with the corresponding coincident β activity [Rad01]. Both activities were obtained through an unfolding procedure so that the contribution of the ^{33}Na decay is determined from the total activity. This resulted in P_n=73(6)%. The predicted three-neutron emission probability is expected to be very small and it was not observed in the present experiment. In order to establish the P_{1n} and P_{2n}

values, which is necessary for obtaining the proper β branches and log *ft* values, the P_{1n}/P_{2n} ratio was evaluated by means of relative γ transition intensities in ^{31}Mg and ^{32}Al β decays. This resulted in P_{1n}/P_{2n} = 3.55(93) which leads to P_{1n} = 47(6) % and P_{2n} = 13(2) %. The previously reported values, P_{1n} = 52(20) % and P_{2n} = 12(5) % [Gui84], are thus confirmed by our present data.

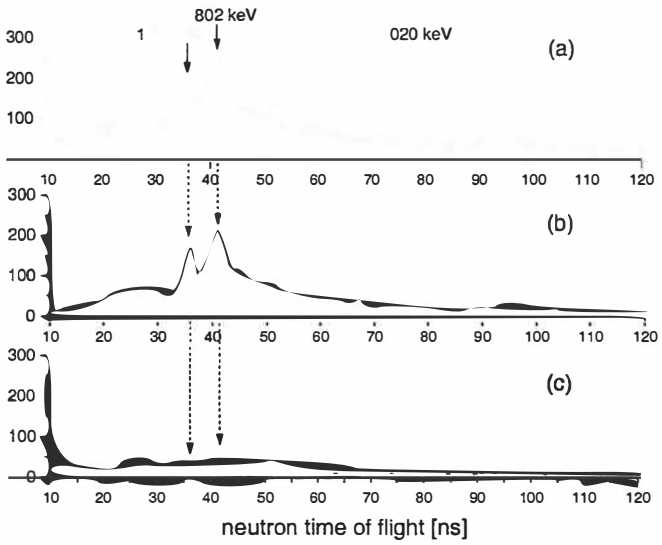

Figure 4.11. Neutron time-of-flight spectra for A=33. The upper spectrum (a) corresponds to β-delayed neutrons appearing in the time window (5-550 ms) after the proton pulse, whereas spectra (b) and (c) correspond to time windows (5-40 ms) and (40-500 ms), respectively.

The β-delayed neutron spectrum, taken at A=33, is reported in Figure 4.11. The time-of-flight spectrum, recorded in the time window (5-550 ms) after the proton pulse, corresponds to spectrum (a). Similarly as in the case of γ spectra, the neutron time-of-flight spectrum has been split up into two time intervals, (5-40 ms) and (40-500 ms), corresponding to spectra (b) and (c), respectively. It appears that the main peaks at 802 keV and 1020 keV are emitted in the first step and thus assigned to the ^{33}Na decay (spectrum b) although the subsequent neutron emitters, ^{33}Mg and ^{32}Mg, have also a maximum of their contribution in this energy range (spectrum c).

The first β decay scheme ^{33}Na has been built according to our new data on β–γ, γ–γ and β-n coincidences and it is shown in Figure 4.12. Among the previously discussed γ transitions, only the 546 keV transition needs some additional arguments, related to its placement in the decay scheme. A careful measurement of the decay rate of 546 keV ($T_{1/2}$ = 7.7(0.9) ms) confirmed the agreement between the half-life of ^{33}Na and as it was mentioned earlier, the 546 keV transition can be associated only with the ^{33}Mg level scheme, and not with ^{32}Mg nor ^{31}Mg. In a case where the 546 keV γ transition would originate directly from a postulated level at 546 keV, it should be preceded by an allowed GT transition. This is also the case for the levels at 705 keV and 1243 keV according to the intensity analysis. However, we do not observe any connecting transitions between this postulated 546 keV level and the 705 keV and 1243 keV levels. As these two latter levels have the same parity, and as the angular momentum difference, ΔJ, should be low for such 1243 keV→ 546 keV or 705 keV → 546 keV transitions, we cannot find any reasonable reason why these connecting transition would not exist, or be beyond our observation. Thus, we rule out the possibility of a level at 546 keV.

In the other interpretation, the 546 keV γ ray would be associated with an unobserved coincident γ transition (energy E_γ), which would be lost in our β-γ coincidence window. The lowest level, besides the ground state, with noticeable β feeding is the 705 keV level. If the 546 keV transition would deexcite this level, i.e. 705 keV = E_γ + 546 keV, it would fix the unobserved transition, decaying to the ground state, to E_γ =159 keV. A transition with such an energy, with multipolarity $L > 1$ involving a parity change, would not fulfil the β-γ coincidence conditions (500 ns) set by the electronics, and therefore would be left unobserved in our β-γ coincidence window. The other level with considerable β feeding is the 1243 keV level, and with a similar argumentation the unobserved transition would introduce a level at E_γ = 697 keV. However, such a transition with $\Delta J \leq 2$, even with change of parity, would not be lost in γ–γ coincidences set by the timing requirements of our experiment. As a conclusion, we are tempted to believe on the first argumentation

and fix the 546 keV transition decaying from the 705 keV level, followed by an unobserved 159 keV transition.

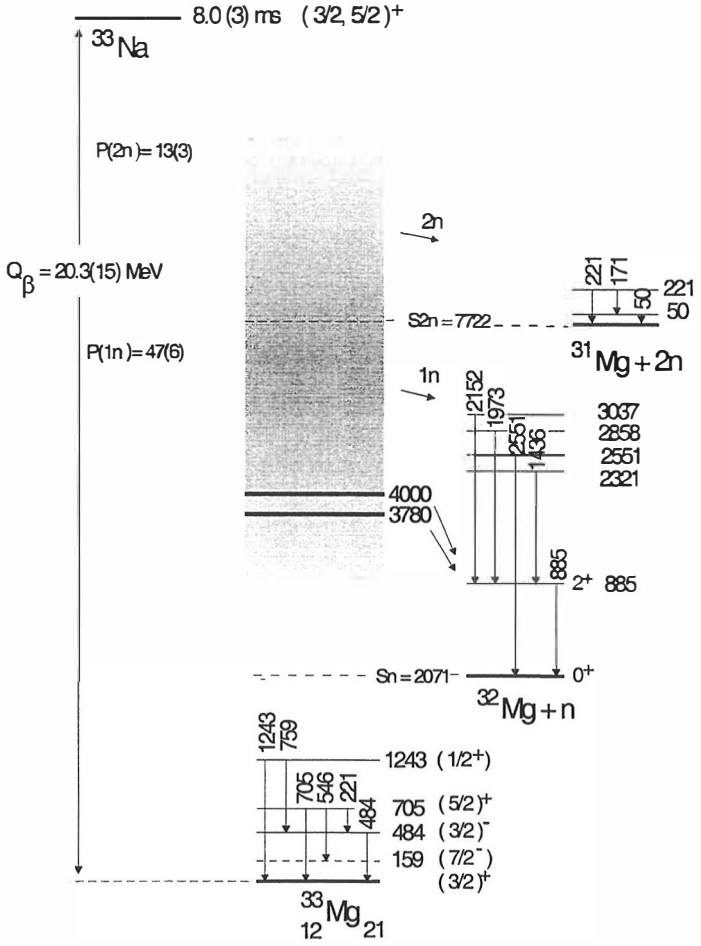

Figure 4.12. β-decay scheme of ^{33}Na.

The β branchings and the log *ft* values for the ground state and excited states are determined according to the level scheme, the deduced absolute γ intensities and the P_{1n} and P_{2n} values (Table 4.6). The Q_β value has been taken from ref. [Aud97], introducing the largest contribution on the errors of log *ft*'s. Three states (g.s., 705 keV and 1243 keV) are described by log *ft* values associated with allowed β transition, and therefore

with positive parities. According to simple shell model considerations, the ground state can be explained with a $(\nu f_{7/2})^2$-$(\nu d_{3/2})^{-1}$ neutron state, resulting in $J^\pi = 3/2^+$, whereas the J for the two excited states with positive parity is limited to $(1/2 - 7/2)^+$.

From similar simple shell model arguments, we expect two negative parity states to be located at low excitation energy, $J^\pi = 7/2^-$ ($f_{7/2}$ neutron) and $J^\pi = 3/2^-$ ($p_{3/2}$ neutron). Relying on the previous argumentation on the excited state at 159 keV, owing to negative parity, the *M2* character of the 159 keV transition suggests for this state $J^\pi = 7/2^-$. Furthermore, with a $J^\pi = 3/2^-$ assignment for the 484 keV level, the 484 keV E1 transition to the g.s.($J^\pi=3/2^+$) dominates the competing *E2* branch to the excited state at E_x=159 keV. With these arguments, we can narrow down the spin and parity assignments of the positive parity states at 705 keV and 1243 keV. The 705 keV level is deexcited by three γ transitions, all of which have comparable intensities. This refers to same multipole order of all three transitions, and more precisely to dipoles due to the observed short lifetimes. Therefore, as the final state have either *J*=3/2 or 7/2, the spin and parity of the 705 keV level is fixed as $J^\pi = 5/2^+$. Finally, since there is no transition observed from the 1243 keV level to the 705 keV and 159 keV levels, we suggest $J^\pi = 1/2^+$ for the 1243 keV level.

Table 4.6. β intensities and log ft values in the ^{33}Na β decay to bound levels in ^{33}Mg

E_x (keV)	I_β (%)	log ft	J^π
0	20(10)	5.27(26)	(3/2)+
158.7 (1)	a)		(7/2-)
484.1 (1)	<1.2	>6.6	(3/2)-
705.03 (9)	15.9(6.2)	5.29(22)	(5/2)+
1242.7 (1)	2.9(1.2)	5.97(25)	(1/2+)

[a] Level energy deduced from the observation of a 594 keV transition, which according to arguments explained in the text deexcites the 705 level and fixes a level at 159 keV energy. No direct β feeding is expected, neither observed, to this level

4.4 Yields of neutron-rich nuclei in superasymmetric fission

The yields of superasymmetric fission products were determined for proton (E_p=30 MeV) induced fission of ^{238}U at IGISOL. The proton beam current of the K=130 cyclotron was kept at a constant level of I = 4 μA. In the case of the rarest short-lived nuclei the activity was moved away in regular time intervals by a tape-drive in order to reduce the activity of the long-lived nuclei. In other cases, the activity was recorded in a saturation mode. The cumulative yields were determined from the radioactivity of the mass separated nuclei, so that the strongest γ rays resulting from the β decay of the nucleus of interest were used. Typically, the γ branching ratios were obtained from literature [Fir96]. In addition, new data on the β decay of very neutron-rich Ni and Cu isotopes have become available recently and the branchings for most of the Ni isotopes and ^{71,73,74}Cu isotopes were obtained from [Mue00a, Mue00b] and [Fra98, Fra00], respectively.

As it was shown in chapter 3.2.2.2, the amount of doubly charged ions of Ba and La in the IGISOL beam could not be lowered in the cooler. Therefore, these ions were not separated by the Wien filter and they resulted in a strong contribution to the γ spectra in masses 68<A<74. Without saying, this made the detailed study of rare Ni and Cu isotopes much harder. As an example, the γ spectrum of A=71 isotopes is shown in Figure 4.13.

The efficiency of the ion guide was checked before each change of mass by observing the yield of ^{112}Rh. These nuclei are strongly produced in proton induced fission and provide a means to monitor the performance of the IGISOL system in a long run. In the present experiment the yield of ^{112}Rh stayed typically at the level of 4000 ions/s, with a constant proton beam current of 4 μA. As a comparison, the yield of ^{112}Rh in the previous superasymmetric fission yield run [Huh97] was 5000 ions/s with a proton beam current of 3 μA. In the previous experiments, however, the cooler was not yet installed to the IGISOL beam line. With the present ion guide configuration one has reached as high as 80 000 ions/s for the yield of ^{112}Rh, with a proton beam current of I_p=16.4 μA [Den98]. As the fission yields do not increase linearly with increasing proton beam current, but

more as the square root of the beam current, the expected yield of ^{112}Rh with I_p=4 μA could easily be 40 000 ions/s. Therefore, in the present experiment the yield was only about 10% of the expected normal yield. This can be explained by an unfortunate leak in the helium line, which resulted in an unusually high impurity level of the helium. The obtained yields for masses A=68, 71, 72, 73, 74, 76, 78 are listed in Table 4.7. They will be discussed in more detail in the discussion chapter, together with future predictions and improvements.

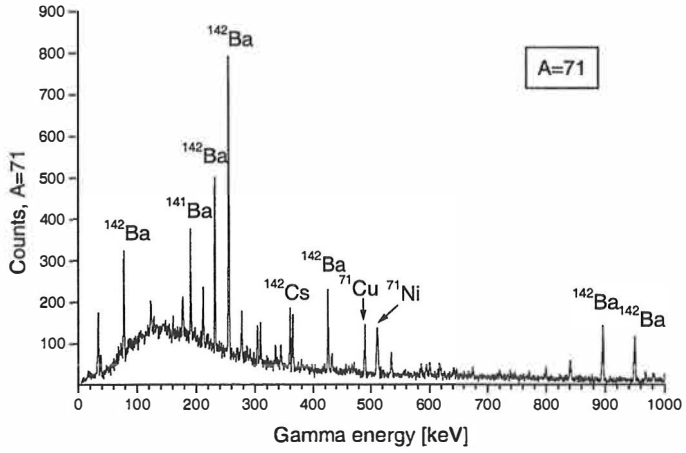

Figure 4.13. The β gated γ ray spectrum recorded at mass A=71. The strongest lines are due to the doubly charged ions.

Table 4.7. Independent fission product yields in atoms/s for elements 27<Z<31 at IGISOL. The yields are measured for the proton (E_p=30 MeV) induced fission of ^{238}U, with a proton beam current of I_p=4 μA.

A	Co	Ni	Cu	Zn	Ga
68	0.3(1)	<0.9	<0.2		
70	<0.5	1.7(4)	3.1(8)		
71		0.7(1)	1.8(4)		
72		0.43(15)	9.5(9)		
74			3.1(2)	10.9(10)	22(4)
76			0.45(4)	35(3)	33(6)
78				4.3(2)	45(3)

5 Discussion

The results of the beta decay measurements performed at ISOLDE will be discussed in the light of shell model calculations, performed by F. Nowacki and E. Caurier. The discussion proceeds in a logical order of the studied nuclei, starting with the N=20 nucleus, ^{34}Si. Then, we move to nearby N=21 nuclei, ^{35}Si and ^{33}Mg, which characterise the transition from spherical to deformed shapes in a clear manner. The order of presentation corresponds to the actual chronological order in which the experimental data were available and analysed, thus providing a distinct guideline for the whole work. At the end, the results of the superasymmetric fission yields will be discussed in comparison with theory and other similar fission measurements, as well as with predictions for future measurements.

5.1 Beta decay of ^{34}Al

5.1.1 *GT transitions in ^{34}Si*

The allowed Gamow-Teller β decay of ^{34}Al ($J^{\pi}_{g.s.} = 4^-$) feeds negative parity states of J=3,4,5 in ^{34}Si, interpreted as particle-hole states. In the work of Baumann *et al.* [Bau89] two negative parity levels at 4.26 MeV and 4.38 MeV were introduced for ^{34}Si, corresponding to more than 50% of the total beta feeding from ^{34}Al. In this work, these two levels were confirmed and, in addition, a third negative parity state at 4.97 MeV was introduced. In order to provide a test for the shell model the Gamow-Teller strength distribution, corresponding to final spin values of J=(3,4,5)$^-$ in ^{34}Si, was computed. The resulting three distributions versus excitation energy in ^{34}Si are shown in the left side of Figure 5.1. A standard quenching factor of 0.77 [Wil84b] was included in the calculations.

Although the strength distribution is mainly peaking around 23 MeV, which is above the Q_β value of 17.1 MeV, most of the beta feeding is connected to only few levels around 4

-5 MeV. Two $J^{\pi}=3^{-}$ levels, situated at 4.35 MeV and 4.75 MeV, fit extremely well with the experimental picture which depicts the power of the present shell model calculations in this region.

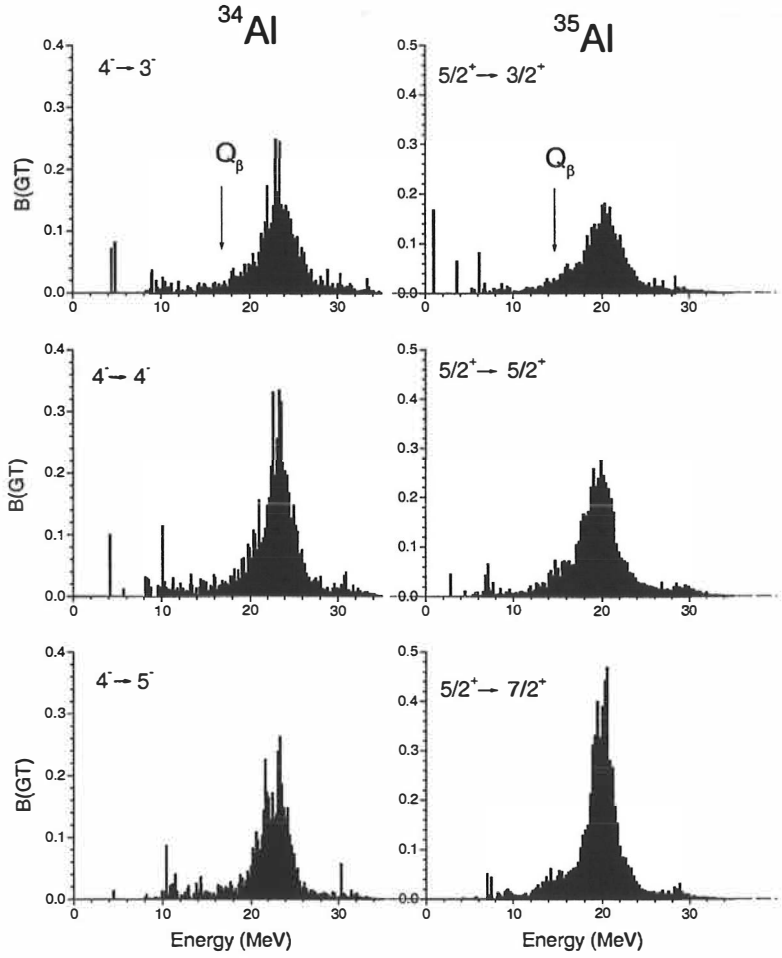

Figure 5.1. Allowed beta decay of ^{34}Al and ^{35}Al. Calculated values of Gamow-Teller strength distribution versus excitation energy for three possible spin values (3^{-}, 4^{-}, 5^{-}) in the final nucleus; ^{34}Si on the left and ^{35}Si on the right.

5.1.2 *Intruder states in ^{34}Si*

A great deal of information, related to the shell structure of N=20 isotones, is revealed by the location of the first two 0^+ and 2^+ states. A previous beta decay study of ^{34}Al described the 0^+_1 ground state of ^{34}Si as a 0p-0h state and the 2^+_1 state at 3326 keV as a 2p-2h intruder state [Bau98]. Furthermore, the second 2^+ state has been tentatively associated with a level at 5.3 MeV [Fif85]. The experimental results already showed that in the present study the 0^+_2 intruder state cannot be determined solely from the experimental data. Instead, we have 1193 keV and 1715 keV gamma transitions, which can be considered as candidates for the $2^+_1 \rightarrow 0^+_2$ transition, as already discussed in the results. In both cases, the $B(E2)(2^+_1 \rightarrow 0^+_2)$ value can be estimated from the measured branching ratios b ($2^+_1 \rightarrow 0^+_1$ and $2^+_1 \rightarrow 0^+_2$) and the experimental value of $B(E2\uparrow)(2^+_1 \rightarrow 0^+_1)$ obtained from Coulomb excitation measurements [Ibb98]. Thus, for the 1193 keV transition the estimated $B(E2)$ is given by

$$B\left(E2\uparrow\right)\left(2_1^+ \rightarrow 0_2^+\right) = \frac{b_{1193}}{b_{3326}}\left(\frac{3326}{1193}\right)^5 B\left(E2\uparrow\right)\left(2_1^+ \rightarrow 0_1^+\right) \qquad (5.1)$$

which after substitution gives $B(E2\uparrow)(2^+_1 \rightarrow 0^+_2)$ = 444(210) $e^2fm^4$for the 1194 keV candidate. Correspondingly, for the 1715 keV candidate the estimate gives $B(E2\uparrow)(2^+_1 \rightarrow 0^+_2)$ = 27(12) e^2fm^4. If we compare these two values to the theoretical predictions of the present work, $B(E2\uparrow)^{th}(2^+_1 \rightarrow 0^+_2)$ = 310 e^2fm^4, we find that the 1193 keV gives a reasonable agreement with the theory. Therefore, we propose that the 0^+_2 state is located at 2133 keV. A summary of the 0^+ and 2^+ states in ^{34}Si is given in Table 5.1, where both theoretical and experimental values for level energies and $B(E2)$ values are given. The agreement between calculations and experimental results is fairly good but it should be noted that a further confirmation for the 0^+_2 state is necessary.

Table 5.1. Experimental and calculated excitation energies (in MeV) in ^{34}Si and transition probabilities (in e^2fm^4). The theoretical values are from this work.

J^π	E_x		Transition	B(E2↑)	
	Theoretical	Experimental		Theoretical	Experimental
0^+_1	0.0	0.0	$0^+_1 \rightarrow 2^+_1$	118	85(33)[a]
0^+_2	2.6	(2.1)	$0^+_2 \rightarrow 2^+_1$	310	444(210)[b]
2^+_1	3.3	3.3	$0^+_1 \rightarrow 2^+_2$	104	<104[a]
2^+_2	5.4	5.3[c]			

[a]From ref.[Ibb98]
[b]Indirect estimates, see text
[c]From ref.[Fif85]

5.2. Beta decay of ^{35}Al

5.2.1 *$f_{7/2}$ and $p_{3/2}$ shell gap; influence on the sd-fp nuclei*

The new results of the beta-decay properties of ^{35}Al and the level scheme of ^{35}Si have been used to modify the effective interaction in shell model calculations. In order to stress the importance of the experimental data of the key-nucleus ^{35}Si a comparison between the old [Ret97] and new calculations according to the new data are presented in Figure 5.2. In this figure the evolution of the $(3/2)^-$ excitation energy in shown for N=21 nuclei, ranging from ^{35}Si (Z=14) to ^{41}Ca (Z=20). The change in these two calculations was due to the modification of the $p_{3/2}s_{1/2}$ and $p_{3/2}d_{3/2}$ terms. It is evident that the previous calculations could not reproduce the excitation energy of the $(3/2)^-$ state in ^{35}Si and modifications on the effective interaction were needed in order to obtain an analogy between theoretical and experimental results.

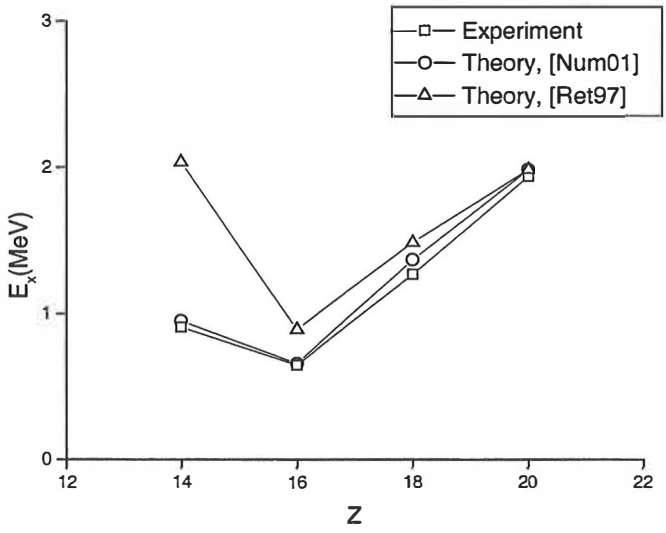

Figure 5.2. Evolution of the (3/2)⁻ state excitation energy in N=21 isotones. The experimental values are compared with two sets of calculations. One set is obtained by using parameters applied for the interaction prior to this experiment (triangles) [Ret97], while the other set uses the single-particle energy for Z=14 obtained in this work (circles) [Num01].

According to the location of the single-particle states in ^{35}Si we can draw conclusions on the evolution of the shell structure in this neutron-rich region. The $(3/2)^-$ state in ^{35}Si can be interpreted as a reduction of the neutron gap between the $f_{7/2}$ and $p_{3/2}$ shells. Although this reduction is moderate it reflects a much more pronounced effect for the N=28 shell gap. This can be illustrated by making once more a comparison between the previous calculation in ref. [Ret97] and according to the new data [Num01]. The comparison is made for Z<20, N>20 nuclei, which are projecting the features of the N=28 shell gap. Table 5.2 contains some calculated electromagnetic-transition properties of six nuclei, compared to experimental data if available.

Table 5.2. Experimental and theoretical excitation energies of the 2_1^+ state in several nuclei and corresponding E2 transitions to the ground state.

Nucleus	$E(2^+)$ (MeV)			$B(E2)$ $(2^+ \rightarrow 0^+)$ e^2fm^4		
	Theoretical		Exp.	Theoretical		Exp
	[Num01]	[Ret97]		[Num01]	[Ret97]	
^{40}Ar	1.37	1.37	1.461	43	43	76(3)[a]
^{40}S	0.98	1.05	0.891(13)[b]	77	75	67(7)[b]
^{42}S	1.02	1.07	0.890(15)[b]	94	93	79(12)[b]
^{46}Ar	1.53	1.65	1.554(26)[b]	80	91	39(8)[b]
^{44}Si	1.22	1.64	1.297(18)[c]	93	79	63(18)[c]
^{42}Si	1.49	2.56		71	49	

[a] See ref.[End79]
[b] See ref.[Sch96]
[c] See ref.[Gla97]

The two calculations barely differ for ^{40}Ar (N=22), ^{40}S (N=24) and ^{42}S(N=26). However, among the N=28 nuclei ^{42}Si comes out as a case where the present calculations diminish the doubly closed shell character in comparison with the previous calculations. In other words, the ^{42}Si nucleus is very sensitive to the chosen interaction, which is just a sign that it lies in the transition region between N=28 gap persistence (^{46}Ar, ^{44}S) and the vanishing of the shell closure (^{40}Mg) [Cau98].

Another aspect related to the reduction of the $f_{7/2}$ - $p_{3/2}$ neutron gap is the shape coexistence at N=28. Recent Coulomb excitation measurements of ^{43}S [Ibb99], as well as the observation of an isomeric state in ^{43}S [Sar99], reveal the shape coexistence of spherical and deformed states in this nucleus. Although most of the deformation effect is due to protons, the reduction of the neutron gap enhances the deformation effect. In Figure 5.3 we show the experimental data on ^{43}S compared to the corresponding calculated values obtained by the new modified interaction.

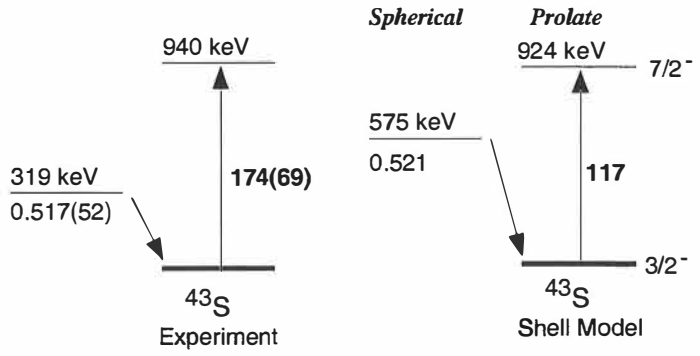

Figure 5.3. Shell model predictions for the first excited states in ^{43}S compared to experimental values ([Ibb99] and [Sar99]). Numbers next to the transitions are B(E2) values in units of e^2fm^4.

5.2.2 *GT transitions in ^{35}Si*

Shell model calculations for the Gamow –Teller strength distribution were made also for the beta decay of ^{35}Al. In the right side of Figure 5.1 the theoretical distributions of the GT strength, corresponding to three possible values of $J^{\pi}=(3/2, 5/2, 7/2)^+$ for the final states in ^{35}Si, are shown. The maximum of the distribution lies around 20 MeV, which is well above the Q_β value 14.3 MeV of ^{35}Al. Regarding our comparison between shell model calculations and experimental data, however, we are interested only in the low energy part of the distribution. Below the one-neutron separation energy, S_n=2.47 MeV, only two levels, $J^{\pi}=(3/2, 5/2)^+$, are predicted to be populated by allowed beta decay. We will see that the calculations are in fact in excellent agreement with the observed level scheme. The predicted $3/2^+$ state with E_{ex}= 952 keV reproduces remarkably well the experimentally confirmed $3/2^+$ level at 974 keV. In addition, the observed $5/2^+$ level at 2.17 MeV finds a clear counterpart from the calculations, although with a slightly higher energy.

5.3. Beta decay of ^{33}Na

The two Si isotopes, ^{34}Si and ^{35}Si, discussed above are clearly situated outside the island of inversion. However, one has to go only to the next lighter N=21 even-Z nucleus and the situation changes. We have already given the level scheme of ^{33}Mg in Figure 4.12 and the beta branches in Table 4.6, which we will now examine in the light of shell model calculations. The effective interaction was adjusted according to the level scheme ^{35}Si and we leave it unchanged. As a consequence of the modified effective interactions, we will first investigate the GT strength distribution of ^{33}Na decay, and then discuss the low lying states of ^{33}Mg.

5.3.1 *GT decay of ^{33}Na*

In order to study the level scheme of ^{33}Mg through beta decay of ^{33}Na, the spin and parity of the ground state in ^{33}Na should be determined. The shell model calculations produce a $0\hbar\omega$ ground state with $J^\pi = 3/2^+$ and a first excited state ($J^\pi = 5/2^+$, $0\hbar\omega$) at 59 keV excitation energy. Since these two states, resulting from three protons sitting at the $d_{5/2}$ orbital, are so close in energy we have to consider both states as possible ground states of ^{33}Na. The second exited state ($J^\pi = 3/2^+$, $2\hbar\omega$) is expected at $E_{ex} = 0.943$ keV and therefore can be excluded as a ground state candidate, as well the other configurations located higher in energy.

Two possible beta decay paths of ^{33}Na can be considered. First, a *sd*-neutron can transform in a *sd*-proton, or alternatively, a *fp*-neutron can transform in a *fp*-proton. These possible decays are schematically illustrated in Figure 5.4. Although the final state in both cases is a $1\hbar\omega$ state, the resulting excitation energy is much higher in the second case ($\nu(fp) \rightarrow \pi(fp)$).

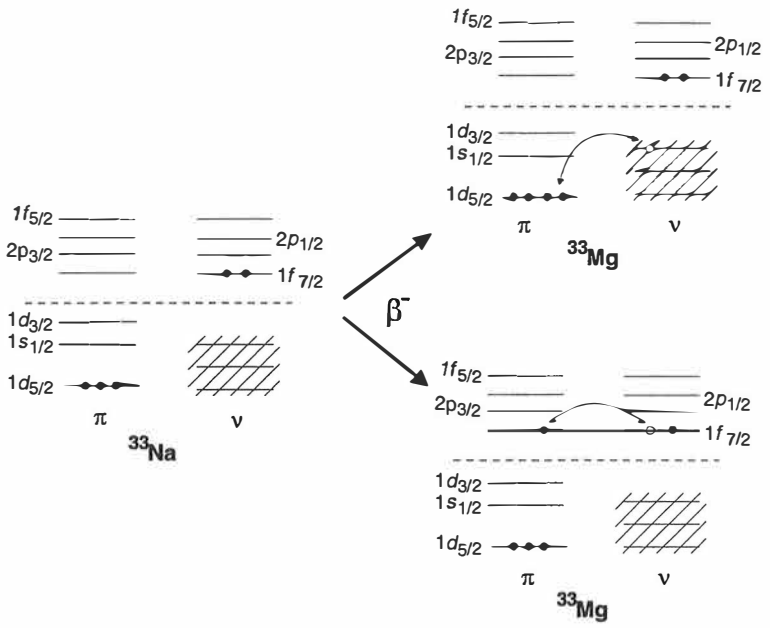

Figure 5.4. Allowed Gamow-Teller decay of ^{33}Na.

The calculated Gamow-Teller strength distribution is plotted in Figure 5.5, both for $J^{\pi} = 3/2^{+}$and $J^{\pi} = 5/2^{+}$ initial states of ^{33}Na. We can observe that the GT distributions in these two cases do not differ much, which can be understood by the similar nature of the mother states. In both cases, there is feeding to the $3/2^{+}$ state of ^{33}Mg, as well as to the first $5/2^{+}$ state at 811 keV, in good agreement with the experiment. Furthermore, there are several levels around 4 MeV, which is above the neutron separation energy of ^{33}Mg (S_{1n} = 2071 keV). These states correspond to the levels which were observed via beta-delayed neutrons. The calculated half-life results in 2.70 ms and 2.76 ms, corresponding to initial states $J^{\pi} = 3/2^{+}$and $J^{\pi} = 5/2^{+}$, respectively. The agreement is reasonable with the experiment ($T_{1/2}^{exp}$ = 8.0(3) ms) and the difference can be understood by the fact that the computed half-life is determined by only some low-energy part of the strength functions.

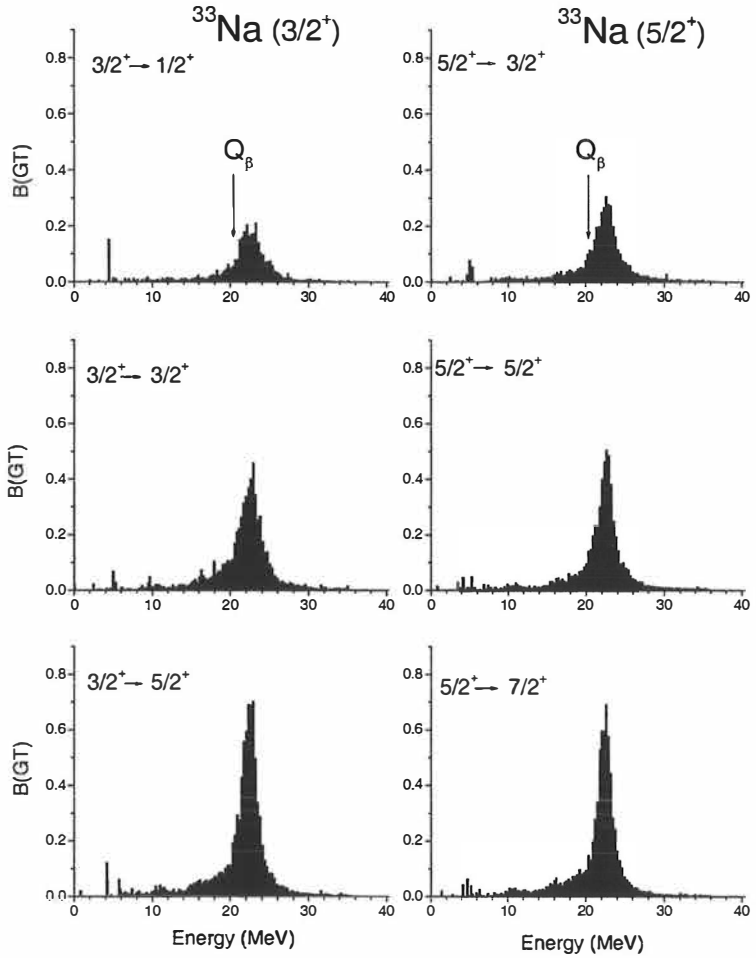

Figure 5.5. Calculated values of the ^{33}Na allowed Gamow-Teller strength distribution versus excitation energy, for three possible spin values in the final nucleus. Distributions for both possible ground state spin assignments of ^{33}Na, 3/2$^+$ and 5/2$^+$, are shown on the left and right, respectively.

5.3.2 *Structure of ^{33}Mg*

A typical feature of the ^{33}Mg spectrum is that different kind of excitations (0ħω, 1ħω and 2ħω) are present both at low and high excitation energies. This is very different to what

was found for ^{35}Si, represented by a much more simple single-particle spectrum. In Figure 5.6 the calculated low energy level scheme of ^{33}Mg is shown, together with the experimentally obtained level scheme. As it was already mentioned during the discussion of the GT strength distribution, the ground state of ^{33}Mg is predicted to be a 1p-1h, J^{π} = $3/2^{+}$, state $((\nu f_{7/2})^{1}, (\nu d_{3/2})^{-1})$. This is in agreement with the experiment, which now provides the first observation of such inversion of states in the island of inversion. However, the comparison between theory and experiment concerning the excited states is not so straightforward, due to the coexitence of different excitations. Still, the rough features can be understood. The calculations take into account also the mixing for 0p-0h and 2p-2h states, which is necessary in order to split the degeneracy of the $7/2^{-}$ states. Such splitting results in lowering the the first $7/2^{-}$ state and introduces a candidate for the long-lived M2 isomer, which was not seen in the present experiment due to restricted coincidence conditions.

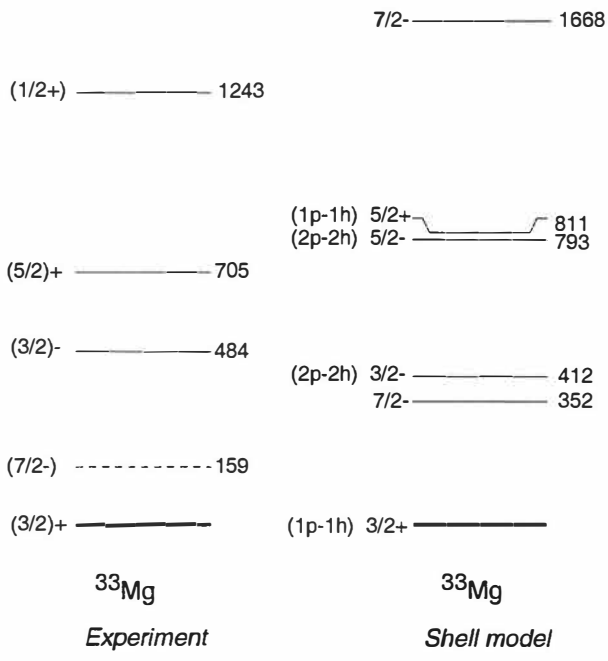

Figure 5.6. Experimental (left) and calculated (right) low energy level scheme of ^{33}Mg. The shell model calculations take also into account for the mixing between 0p-0h and 2p2h configurations.

5.4 Production of neutron-rich nuclei close to ^{78}Ni

The obtained yields of superasymmetric fission products can be used as an estimate for the production of exotic isotopes, such as doubly-magic ^{78}Ni, at IGISOL. The experimental yields have been analysed in the framework of a theoretical model, proposed in ref. [Kar91, Jau94], which has been later modified [Huh97]. This model, which calculates mass and independent fission product yields after emission of neutrons from excited fission fragments, takes into account the influence of nuclear shells, the charge polarisation and odd-even effects in charge and mass distributions. The total mass distribution is a contribution from four different fission modes, one symmetric mode and three asymmetric modes. The symmetric fission mode is approximated by a single Gaussian distribution, while the three asymmetric fission modes are each described by a pair of Gaussian distributions. The previous study of fission yields at intermediate excitation energy [Huh97] concluded that the contribution of the most asymmetric component is significant near the nuclear shells Z=28 and N=50.

The independent fission yields obtained in the present work, which were already given in Table 4.7, are shown in Figure 5.7 as points and error bars in units of *atoms/s*. Theoretical isotopic yields are shown as dotted lines for Co, Ni, Cu, Zn and Ga, which can be converted to cross sectional units of *mb* by multiplying with scale factors shown in brackets. The parameters of the model have been fitted to experimental data obtained from fission yield experiments in Leuven [Kru00] and they have not been changed according to these new data. Instead, the calculated distributions for each element have been multiplied with the scale factor in order to fit best with the experimental distribution.

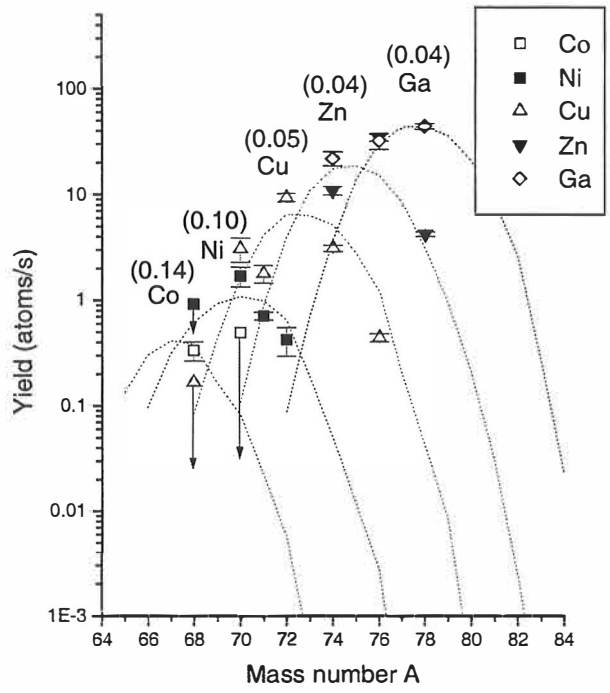

Figure 5.7. Experimental independent yields (points with error bars) and calculated isotopic distributions (dotted lines) of Co, Ni, Cu, Zn and Ga in 30 MeV proton induced fission of ^{238}U. The numbers above each element give the scale factor mb/(at/s).

The yield values are comparable with the previous measurement by Huhta et al., in which yields for masses 71<A<82 in 25 MeV proton induced fission of ^{238}U at IGISOL were deduced. This can be expected, since the proton energy differs only by 5 MeV, and the proton beam current only by 20% (I_p=3 μA in ref. [Huh97]). The most relevant difference from an analysis point of view, however, comes from new available data of several Ni isotopes. Previously, ^{71}Ni was the only Ni isotope for which the yield could be determined according to characteristic γ rays, which was also only the upper limit estimate. At that time, the theoretical prediction for the average distribution of Ni gave A_{av} = 71.23. A disagreement between the model and experiment was found later in fission yield experiments in Leuven [Fra98] where a study of several Ni isotopes resulted in A_{av} = 69.5(3). Since then, the model parameters have been modified and presently the average of the theoretical Ni isotopic distribution lies at A=69.93 [Rub01]. According to

the new information of several Ni β decay schemes and γ intensities [Fra98, Mue00a, Mue00b], we have obtained yield values for four Ni isotopes at IGISOL. With the present results, the average is observed around A = 70, in agreement with the model and the data from Leuven. The fission yield measurement in Leuven, using a laser-ionisation isotope separation on-line method IGLIS, have resulted in an extensive study of isotopic distributions of Co, Ni and Cu products [Mue00a, Kru00]. As a comparison, the yield of ^{71}Ni in Leuven was measured to be 12(5) at/μC [Mue00a].

In order to make a prediction for the future production yield of ^{78}Ni at IGISOL, a few corrections should be made to the present yields. As it was mentioned earlier in the results, the conditions in the ion-guide helium gas in the present experiment resulted in about 90% loss in yield, compared to the normal conditions. Normal conditions are referred to as 20 000 ions/s for ^{112}Rh yield with 1 μA proton beam current, whereas in the present work the yield was only 4000 ions with 4 μA proton beam current [Den98]. Nowadays, the fission yields increase as the square root of the increasing beam current, so that the present results correspond to about 2000 ions/s of ^{112}Rh with 1 μA proton beam. Along the improvements in the ion guide and in the transmission between the ion guide and the skimmer, the expectation is to obtain a system which allows a linear increase in fission yield with a linear increase in proton beam current. With the present H^- ion source at the Department of Physics, University of Jyväskylä, the current of the 30 MeV proton beam has reached a level as high as I_p=50 μA, which anticipates a significant increase in yield in the future. Furthermore, the present transmission of the cooler in the IGISOL beam line is around 35%, which could be expected to increase to 100% percent. To summarise these improvements, the fission yields could be increased by a factor of 750, compared to the yields presented in this work. Therefore, as the extrapolation of the ^{78}Ni yield, based on calculations (Figure 5.7) gives $7 \cdot 10^{-6}$ ions/s, the prediction for future yields gives 450 ions/day, according to the above mentioned technical improvements. The inverse kinematic reaction studies at GSI have so far reached a production rate of only 3 ions/day for ^{78}Ni [Eng95], which serves merely as a way of identification but enables no spectroscopic study.

Even though one would obtain a reasonable yield for the production of exotic nuclei, the presence of different kind of contaminants in the mass-separated beam may easily spoil the experiment. It was already shown that the presence of doubly charged ions severely harms the spectroscopic study of superasymmetric fission products and that a Wien velocity filter was designed to overcome this problem at IGISOL. Although the present conditions in the cooler were not suitable for the charge exchange reaction to occur in light fission products, a proper choice of impurity gas would result in the wanted effect.

Furthermore, a present project to include a longitudinal penning trap connected to the IGISOL beam line will allow an isobaric separation of the beam. This will eliminate the presence of isobaric isotopes of larger atomic number, which have much larger fission cross sections, and therefore provides a clean beam of exotic nuclei. Also, in case the Wien filter in not used, the separation of doubly charged ions is possible with the Penning trap. As an example, the separation of ^{142}Ba (q=2+) from ^{71}Ni (q=1+) requires a mass resolution of about 10^{-4}, which correspond to a purification time of roughly 100 ms in the Penning trap.

Although a lot of effort is put on efficient detection techniques, the choice of the reaction itself is a factor that can give a major influence on the yields. The choice of the target and the projectile can slightly shift the Gaussian distribution of the element yields, which may considerably increase the yields for the very neutron-rich nuclei at the steep slopes of the Gaussians. For example, from Figure 5.7 one can estimated that for Ni isotopes a change of 1.0 mass units in A_{av} to the higher masses corresponds to an increase of a factor of 10 in yield for ^{78}Ni. This requires a systematic study of suitable reactions, such as neutron or deuteron induced fission of ^{238}U or ^{232}Th. Such studies have been performed at HENDES [Trz97], which is designed for neutron and light charged particle detection in coincidence with fission fragments. Mass distributions of fission products have been measured for proton induced fission of ^{238}U and ^{232}Th, with varying proton energies [Trz98]. Although this provides an efficient way to detect the fission fragments, it still doesn't allow the identification of the atomic number of the nuclei, which eventually is necessary in order to predict the yields of the very neutron-rich nuclei.

6 Summary

This thesis has concentrated on the study of neutron-rich nuclei and on the production of such nuclei in fission. We have been able to bring valuable new spectroscopic information through detailed study of beta decay schemes of nuclei around the so-called "island of inversion" as well as to delineate the possibilities to use intermediate energy proton induced fission as means to produce exotic nuclei near the doubly-magic ^{78}Ni isotope.

Two experiments at the ISOLDE facility at CERN were dedicated to the β decay study of ^{34}Al, ^{35}Al and ^{33}Na. The level schemes of their daughter nuclei have been built through observation of β-γ, β-γ-γ, β-*n* and β-γ-*n* coincidences. The level scheme of ^{34}Si was partly known prior to this work, and the previously reported levels were confirmed together with 4 new identified γ transitions. The energy for the first excited 0_2^+ state in ^{34}Si has been proposed, which can serve as a test for shell model calculations. However, the most important piece of information comes from the first description of the level structures of the isotopes ^{35}Si and ^{33}Mg (N=21). The low energy level schemes of ^{35}Si and ^{33}Mg are given in Figure 6.1, as continuation of the N=21 systematics starting from ^{41}Ca. In addition, the half-lives of all studied nuclei have been newly determined, resulting in a considerable improvement for the half-life value of ^{35}Si ($T_{1/2}$ =38.4(4)ms).

The experimental data have been compared with the shell model calculations. The GT distributions were calculated for the allowed beta decay of ^{34}Al, corresponding to three possible values of J^{π}= (3,4,5)$^-$ for the final states in ^{34}Si. We find that the theoretical results are in excellent agreement with the experimentally confirmed allowed β decay of ^{34}Al, populating the low energy levels of ^{34}Si. The level scheme of ^{35}Si has revealed the location of the single-particle $p_{3/2}$ and $d_{3/2}$ states which give insight to the interplay between *sd*- and *fp*-shells. Parts of the effective interactions in shell model calculations have been modified according to the low energy level scheme of ^{35}Si. The results of these calculations can be interpreted as a reduction of the neutron gap between the $f_{7/2}$ and $p_{3/2}$

shells. In addition, the calculated GT strength distributions according to the *sd-fp* shell-model calculations are compared with the observed allowed transitions of the ^{35}Al decay. The $(3/2)^+$ state at 974 keV is remarkable well reproduced, corresponding to a large fraction of the allowed decay.

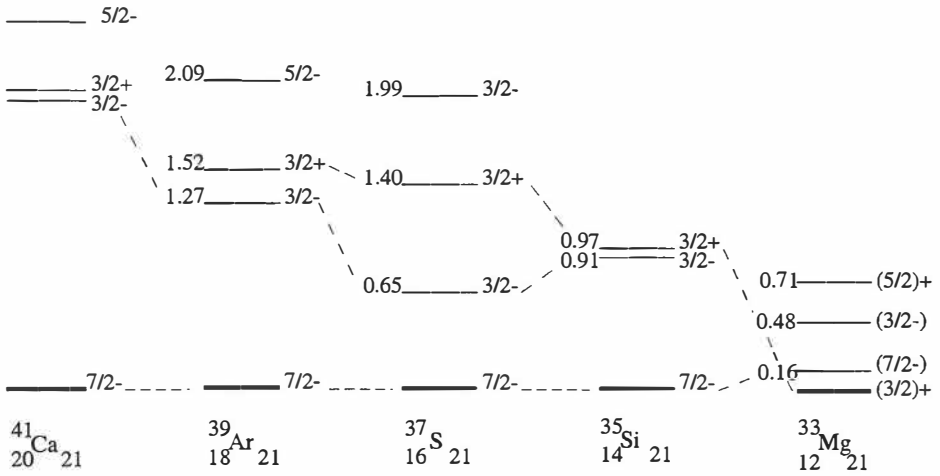

Figure 6.1. N=21 systematics.

The low energy level systematics of N=21 nuclei are shown in Figure 6.1, where the two lightest isotopes are the results of this work. As it is seen from this figure, the ground state of ^{33}Mg has been now experimentally assigned as $J^\pi = 3/2^+$, where as for heavier N=21 even-Z nuclei (^{41}Ca - ^{35}Si) the ground state assignment gives $J^\pi = 7/2^-$. In calculating the GT strength distribution of ^{33}Na, two possible ground state configurations, $3/2^+$ had $5/2^+$, had to be considered. Both cases reproduced the experimental situation, where most of the beta feeding is to the $3/2^+$ ground state and $5/2^+$ excited state, interpreted as 1p-1h states. This is a clear manifestation of the island of inversion. In addition, the observed negative parity $3/2^-$ state finds a clear counterpart in the shell model calculations as a 2p-2h state and a candidate for the long-lived 159 keV state appears in the calculations assuming a mixing between $0\hbar\omega$ and $2\hbar\omega$ configurations.

The yields for 30 MeV proton induced fission of ^{238}U were investigated at the IGISOL mass separator facility at the Department of Physics in Jyväskylä. These yields have been analysed in the framework of a fission model, through which extrapolations for the yields of rare neutron-rich nuclei can be made. Special interest is connected to the isotopic yields of nickel, which provide points of comparison for the estimated production yield for the doubly-magic ^{78}Ni. Future technical improvements at IGISOL have been discussed and an estimate of 450 ions/day for ^{78}Ni is given, showing the power of superasymmetric fission as a mechanism to produce this exotic nucleus.

The study of fission yields at IGISOL initiated also a development of a velocity filter. Such a device was designed to separate the doubly charged ions from the singly charged ones in the beam of radioactive ions. In order to achieve the desired performance of the Wien filter the charge exchange process $2+ \rightarrow 1+$, taking place in the cooler, was studied. We observed the charge exchange process for the doubly charged ^{112}Rh ions, as an effect by N_2 impurity molecules in the cooler. However, the same conditions were not favourable for the doubly charged Ba and La isotopes which are strongly present in the mass separated beam of A≈70 fission products. In order to make the charge exchange process achievable for a specific elements, a further study of impurity molecules is still needed.

As a final conclusion, we have shown an example of beta decay measurements which have provided a powerful tool to investigate neutron-rich nuclei in the region of the island of inversion. It has also become evident that the shell model calculations are able to reproduce extremely well the features connected to the *sd-fp* shell interfaces. Finally, we conclude that the observation of doubly magic ^{78}Ni is an ambitious challenge for the future, but indeed attainable along the improvements at IGISOL.

References

[Aud97] G. Audi, O. Bersillon, J. Blachot and A.H. Wapstra, Nucl. Phys A **624** (1997) 1

[Bau89] P. Baumann, A. Huck, G. Klotz, A. Knipper, G. Walter, G. Marguier, H.L. Ravn, C. Richard-Serre, A. Poves and J. Retamosa, Phys. Lett. B **228** (1989) 458

[Bau98] P. Baumann, M. Bounajma, F. Didierjean, A. Huck, A. Knipper, M. Ramdhane, G. Walter, G. Marguier, C. Richard-Serre, B.A. Brown, and the ISOLDE Collaboration, Phys. Rev. C **58** (1998) 1970

[Baz88] D. Bazin *et al.*, AIP Conf. Proc. 5th Int. Conf. Nuclei far from Stability, Rosseau Lake, Canada (1987), Ed. I.S. Towner, p.722 (1988)

[Ber95] M. Bernas, F. Ameil, P. Armbruster, S. Czajkowski, Ph. Dessagne, C. Donzaud, Ch. Engelmann, H. Geissel, A. Heinz, Z. Janas, C. Kozhuharov, Ch. Miehé, G. Munzenberg, M. Pfutzner, C. Rohl, W. Schwab, C. Stephan, K. Summerer, L. Tassan-Got, B. Voss, Proc. Intern. Conf on Exotic Nuclei and Atomic Masses, Arles, France, June 19-23, 1995, p.481 (1995)

[Bil98] J.H. Billen and L.M. Young, Poisson Superfish, LA-UR-96-1834, Los Alamos National Laboratory, 1998

[Bou96] M. Bounajma, Thesis (1996) Strasbourg, CRN 96-43

[Bru77] P.J. Brussaard, P.W. M. Glaudemans, Shell Model Applications in Nuclear Spectroscopy (North-Holland, New York, 1977)

[Cam75] X. Campi, H. Flocard, A.K. Kerman and S. Koonin, Nucl. Phys A **251** (1975) 193

[Cau98] E. Caurier, F. Nowacki, A. Poves and J. Retamosa, Phys. Rev. C **58** (1998) 2033

[Den97] P. Dendooven, Nucl. Instr. and Meth. in Physics Reseach B **126** (1997) 182

[Den98] P. Dendooven, S. Hankonen, A. Honkanen, M. Huhta, J. Huikari, A. Jokinen, V.S. Kolhinen, G. Lhersonneau, A. Nieminen, M. Oinonen, H. Penttilä, K. Peräjärvi, J.C. Wang and J. Äystö, in Nuclear Fission and Fission-Product Spectroscopy, G. Fioni *et al.* (eds.), AIP CP447, 1998, p.135

[Det79] C. Detraz, D. Guillemaud, G. Huber, R. Klapisch, M. Langevin, F. Naulin, C. Thibault, L.C. Carraz and F. Touchard, Phys. Rev. C **19** (1979) 171

[Det83] C. Detraz, M. Langevin, M.C. Goffri-Kouassi, D. Guillemaud, M. Epherre, G. Audi, C. Thibault, F. Touchard, Nucl. Phys. A **394**, 378 (1983)

[Duf86] J.P. Dufour, R. Del Moral, A. Fleury, F. Hubert, D. Jean, M.S. Pravikoff, H.Delagrange, H. Geissel, K.-H. Schmidtet, Z. Phys. A **324** (1986) 487

[End79] P.M. Endt, At. Data Nucl. Tables **23** (1979) 3

[End93] P.M. Endt, At. Data Nucl. Data Tables **55** (1993) 17

[Eng95] Ch. Engelmann, F. Ameil, P. Armbruster, M. Bernas, S. Czajkowski, Ph. Dessagne, C. Donzaud, H. Geissel, A. Heinz, Z. Janas, C. Kozhuharov, Ch. Miehe, G. Munzenberg, M. Pfutzner, C. Rohl, W. Schwab, C. Stephan, K. Summerer, L. Tassan-Got, B. Voss, Z. Phys. A **352** (1995) 351

[Fif85] L.K. Fifield, C.L. Woods, R.A. Bark, P.V. Drumm and M.A.C. Hotchkis, Nucl. Phys. A **440** (1985) 531

[For94] B. Fornal, R.H. Mayer, I.G. Bearden, Ph. Benet, R. Broda, P.J. Daly, Z.W. Grabowski, I. Ahmad, M.P. Carpenter, P.B. Fernandez, R.V.F. Janssens, T.L. Khoo, T. Lauritsen, E.F. Moore, M. Drigertet, Phys. Rev. C **49** (1994) 2413

[For97] B. Fornal, R. Broda, W. Królas, Pawłat, J. Wrzesinski, D. Bazzacco, D. Fabris, S. Lunardi, C. Rossi Alvarez, G. Viesti, G. de Angelis, M. Cinausero, D. R. Napoli and Z.W. Grabowski, Phys. Rev. C **55** (1997) 762

[Fir96] R.B. Firestone, V.S. Shirley, Table of Isotopes, 8^{th} ed. (Wiley, New York, 1996)

[Fra98] S. Franchoo, M. Huyse, K. Kruglov, Y. Kudryavtsev, W.F. Mueller, R. Raabe, I. Reusen, P. Van Dupper, J. Van Roosbroeck, L. Vermeeren and A. Wöhr, Phys. Rev. Lett. **81** (1998) 3100

[Fra00] S. Franchoo (private communication)

[Fuk92] N. Fukunishi, T. Otsuka and T. Sebe, Phys. Lett. B **296** (1992) 279

[Gla97] T. Glasmacher, B.A. Brown, M.J. Chromik, P.D. Cottle, M. Fauerbach, R.W. Ibbotson, K.W. Kemper, D.J. Morrissey, H. Scheit, D.W. Sklenicka, M. Steiner, Phys Lett. B **395** (1997) 163

[Gil87] A. Gillibert, W. Mittig, L. Bieanchi, A. Cunsolo, B. fernandez, A. Foti, J. Gastebois, Y. Schutz and C. Stephan, Phys. Lett. B **192** (1987) 39

[Gui84] D. Guillemaud-Mueller, C. Detraz, M. Langevin, F. Naulin, M. de Saint-Simon, C. Thibault, F. Touchard and M. Epherre, Nucl. Phys. A **426** (1984) 37

[Hax49] O. Haxel, J.H.D. Jensen and H.E. Suess, Phys. Rev. **75** (1949) 1766

[Hey91] K. Heyde and J.L. Wood, J. Phys. G 17 (1991) 135

[Huh97] M. Huhta, P. Dendooven, A. Honkanen, A. Jokinen, G. Lhersonneau, M. Oinonen, H. Penttilä, K. Peräjärvi, V.A. Rubchenya and J. Äystö, Phys. Lett. B **405** (1997) 230

[Ibb98] R.W. Ibbotson, T. Glasmacher, B.A. Brown, L. Chen, M.J. Chromick, P.D. Cottle, M. Fauerbach, K.W. Kemper, D.J. Morrissey, H. Scheit and M. Thoennessen, Phys. Rev. Lett. **80** (1998) 2081

[Ibb99] R.W. Ibbotson, T. Glasmacher, P.F. Mantica and H. Scheit, Phys. Rev. C **59** (1999) 642

[Jau94] P.P. Jauho, A. Jokinen, M. Leino, J.M. Parmonen, H. Penttilä , J. Äystö, K. Eskola and V.A. Rubchenya., Phys. Rev. C **49** (1994) 2036

[Kah69] S. Kahana, H.C. Lee and C.K. Scott, Phys. Rev. 180 (1969) 180

[Kan95] J. Kantele, Handbook of Nuclear Spectrometry, Academic Press Inc., London, 1995

[Kar91] E. Karttunen, M. Brenner, V.A. Rubchenya, S.A. Egorov, V.B. Funschtein, V.A. Jakovlev and Yu.A. Selitskiy, Nucl. Sci. Engin. **109** (1991) 350

[Klo93] G. Klotz, P. Baumann, M. Bounajma, A. Huck, A. Knipper, G. Walter, G. Marguier, C. Richard-Serre, A. Poves and J. Retamosa, Phys. Rev. C **47** (1993) 2502

[Kru00] K. Kruglov, B. Bruyneel, S. Dean *et al.*, in Proceedings of 5th International Conference on Radioactive Nuclear Beams, RNB 2000, Divonne, France, 3-8 April, 2000, Nucl. Phys A, in press

[Kug92] E. Kugler, D. Fiander, B. Jonson, H. Haas, A. Przewloka, H.L. Ravn, D.J. Simon, K. Zimmer and the ISOLDE collaboration, Nucl. Instr. And Meth. B **70** (1992) 41

[Lan84] M. Langevin, C. Detraz, D. Guillemaud-Mueller, A.C. Mueller, C. Thibault, F. Touchard, M. Epherre, Nucl. Phys. A **414** (1984) 151

[Lei91] M. Leino, P.P. Jauho, J. Äystö, P. Decrock, P. Dendooven, K. Eskola, M. Huyse, A. Jokinen, J.M- Parmonen, H. Penttilä, G. Reusen, P. Taskinen, P. Van Duppen and J. Wauters, Phys. Rev. C 44 (1991) 336

[Let97] J. Lettry, R. Catherall, P. Drumm, P. Van Duppen, A.H.M. Evensen, G.J. Focker, A. Jokinen, O.C. Jonson, E. Kugler, H. Ravn and ISOLDE Collaboration, Nucl. Instrum. and Meth. in Phys. Res. B **126** (1997) 130

[Lew89] M. Lewitowicz et al., Nucl. Phys. A496 (1989) 477 and A.C. Mueller et al., Z. Phys. A **330** (1988) 63

[Lew94] M. Lewitowicz, R. Anne, G. Auger, D. Bazin, C. Borcea, V. Borrel, J.M. Corre, T. Dorfler, A. Fomichov, R. Grzywacz, D. Guillemaud-Mueller, R. Hue, M. Huyse, Z. Janas, H. Keller, S. Lukyanov, A.C. Mueller, Yu. Penionzhkevich, M. Pfutzner, F. Pougheon, K. Rykaczewski, M.G. Saint-Laurent, K. Schmidt, W.D. Schmidt-Ott, O. Sorlin, J. Szerypo, O. Tarasov, J. Wauters, J. Zylicz, Phys. Lett. B **332** (1194) 20

[Lin83] W. Lindinger, Physica Scripta. T **3** (1983) 115

[May84] W.A. Mayer, W. Henning, R. Holzwarth, H.J. Körner, G. Korschinek, W.U. Mayer, G. Rosner and H.J. Scheerer, Z. Phys. A **319** (1984) 287

[Mos89] M. Moszynski, J.H. Bjerregard, J.J. Gaarshje, B. Herskind, P. Knudsen and G. Sletten, Nucl. Instrum. and Meth. A **280** (1989) 73

[Mot95] T. Motobayashi, Y. Ikeda, Y. Ando, K. Ieki, M. Inoue, N. Iwasa, T. Kikuchi, M. Kurokawa, S. Moriya, S. Ogawa, H. Murakami, S, Shimoura, Y. Yanagisawa, T. Nakamura, Y. Watanabe, M. Ishihara, T. Teranishi, H. Okuno and R.F. Casten, Phys. Lett. B **346** (1995) 9

[Mue00a] W.F. Mueller, B. Bruyneel, S. Franchoo, M. Huyse, J. Kurpeta, K. Kriglov, Y. Kudryantsev, N.V.S.V. Prasad, R. Raabe, I. Reusen, P. Van Duppen, J. Van Roosbroeck, L. Vermeeren and L. Weissman, Phys. Rev. C **61** (2000) 054308

[Mue00b] W. Mueller (private communication)

[Nie00] A. Nieminen, J. Huikari, A. Jokinen, J. Äystö, P. Campbell, E.C.A. Cochrane and the EXOTRAPS collaboration, Nucl. Instr. Meth. Phys. Res., in press

[Num01] S. Nummela, P. Baumann, E. Caurier, P. Dessagne, A. Jokinen, A. Knipper, G. Le Scornet, C. Miehé, F. Nowacki, M. Oinonen, Z. Radivojevic, M. Ramdhane, G. Walter, J. Äystö and the ISOLDE Collaboration, Phys Rev C **63** (2001) 044316

[Ots96] T. Otsuka and N. Fukunishi, Phys. Rep. **264** (1996) 297

[Pen97] H. Penttilä, P. Dendooven, A. Honkanen, M. Huhta, P.P. Jauho, A. Jokinen, G. Lhersonneau, M. Oinonen, J.-M. Parmonen, K. Peräjärvi and J. Äystö, Nucl. Instrum. and Meth. B **126** (1997) 213

[Pov81] A. Poves and A. Zuker, Phys. Rep. **70** (1981) 4

[Pov94] A. Poves and J. Retamosa, Phys. Lett. B **184** (1987) 311, Nucl. Phys. A **571** (1994) 221

[Pri00a] B.V. Pritychenko, T. Glasmacher, B.A. Brown, P.D. Cottle, R.W. Ibbotson, K.W. Kemper and H Scheit, MSUCL-1157, June-2000

[Pri00b] B.V. Pritychenko, T. Glasmacher, B.A. Brown, P.D. Cottle, R.W. Ibbotson, K.W. Kemper, L.A. Riley and H Scheit, MSUCL-1157, June-2000

[Pri01] B.V. Pritychenko, T. Glasmacher, B.A. Brown, P.D. Cottle, R.W. Ibbotson, K.W. Kemper and H. Scheit, MSUCL-1185, submitted to Phys. Rev. C

[Rad01] Z. Radivojedic, P. Baumann, E. Caurier, J. Cederkäll, S. Courtin, Ph. Dessagne, A. Jokinen, A. Knipper, G. Le Scornet, V. Lyapin, Ch. Miehé, F. Nowacki, S. Nummela, M. Oinonen, E. Poirier, M. Ramdhane, W.H. Trzaska, G. Walter, J. Äystö and the ISOLDE Collaboration, submitted to Nucl. Instrum. and Meth. A.

[Ree95] P.L. Reeder, Y. Kim, W.K. Hensley, H.S. Miley, R.A. Warner, Z.Y. Zhou, D.J. Vieira, J.M. Wouters and H.L. Siefert, in Proceedings of the International Conference on Exotic Nuclei and Atomic Masses, Arles, France, 1995, p. 587, edited by M. de Saint Simon and O. Sorlin

[Ret97] J. Retamosa, E. Caurier, F. Nowacki and A. Poves, Phys. Rev. C **55** (1997) 1266

[Rub01] V. Rubchenya (private communication)

[Sar99] F. Sarazin, H. Savajols, W. Mittig, P. Roussel-Chomaz, G. Auger, D. Baiborodin, A.V. Belozyorov, C. Borcea, Z. Dlouhy, A. Gillibert, A.S. Lalleman, M. Lewitowics, S.M. Lukyanov, F. Nowacki, F. de Oliveira, N. Orr, Y.E. Penionzhkevich, Z. Ren, D. Ridikas, H. Sakurai, O. Tarasov and A. de Vismes, Wintermeeting in Bormio, 1999

[Sar00] F. Sarazin, H. Savajols, W. Mittig, F. Nowacki, N.A. Orr, Z. Ren, P. Roussel-Chomaz, G. Auger, D. Baiborodin, A.V. Belozyorov, C. Borcea, E. Caurier, Z. Dlouhý, A. Gillibert, A.S. Lalleman, M. Lewitowicz, S.M. Lukyanov, F. de Oliveira, Y.E. Penionzhkevich, D. Ridikas, H. Sakurai, O. Tarasov and A. de Vismes, Phys. Rev. Lett. **84** (2000) 5062

[Sch96] H. Scheit, T. Glasmacher, B.A. Brown, J.A. Brown, P.D. Cottle, P.G. Hansen, R. Harkewicz, M. Hellstrom, R.W. Ibbotson, J.K. Jewell, K.W.

Kemper, D.J. Morrissey, M. Steiner, P. Thirolf, M. Thoennessen, Phys. Rev. Lett. **77** (1996) 3967

[Thi75] C. Thibault, R. Klapisch, C. Rigaud, A.M. Poskanzer, R. Prieels, L. Lessard and W. Reisdorf, Phys. Rev. C **12** (1975) 644

[Tow95] I.S. Towner, E. Hagberg, J.C. Hardy, V.T. Koslowsky and G. Savards, Proc. of the 1st International Conference of Exotic Nuclei and Atomic Masses ENAM-95, Arles, France, June 19-23 (1995)

[Trz97] W.H. Trzaska, V.A. Rubchenya, A.A. Alexandrov, I.D. Alkhazov, J. Äystö, J. von Kalben, S.V. Khlebnikov, A.V. Kuznetsov, V.G. Lyapin, V.E. Makarenko, Yu. Moltchanov, M. Mutterer, O.I. Ossetrov, G. Otroshtchenko, H.-G. Ortlepp, Yu.E. Penionzhkevich, Yu. V. Pyatkov, G.P. Tiourine and D.N. Vakhtin, CP392, Application of Accelerators in Research and Industry, edited by J.L. Duggan and I.L. Morgan, AIP Press, New York, 1997

[Trz98] W.H. Trzaska, V.A. Rubchenya, J. Äystö, Z. Radivojevic, D.N. Vakhtin, I.D. Alkhazov, A. Evsenin, S.V. Khlebnikov, A.V. Kuznetsov, V.G. Lyapin, O.I. Ossetrov, G.P. Tiourine, A.A. Alexandrov, Yu.E. Penionzhkevich, Yu.G. Sobolev and M. Mutterer, Il Nuovo Cimento, Vol. **111** A, N. 8-9 (1998) 1055

[War87] E.K. Warburton and J.A. Becker, Phys. Rev. C **35** (1987) 1851

[War 88] E.K. Warburton and J.A. Becker, Phys. Rev. C **37** (1988) 754

[War90] E.K. Warburton, J.A. Becker and B.A. Brown, Phys. Rev. C **41** (1990) 1147

[Wat81] A. Watt, R.P. Singhal, M.H. Storm and R.R. Whitehead, J. Phys. G **7** (1981) L145

[Wea74] Handbook of Chemistry and Physics, 55th edition, edited by R.C. Weast, CRC Press, Cleveland, 1974

[Wil69] D.H. Wilkinson, Nucl. Phys. A133 (1969) and Nucl. Instr. Meth. **82** (1970)

[Wil83] B.H. Wildenthal, M.S. Curtin and B.A. Brown, Phys. Rev, C **28** (1983) 1343

[Wil84] B.H. Wildenthal, Prog. Part. Nucl. Phys. **11** (1984) 5

[Woo86] C.L. Woods, Nucl. Phys. A **451** (1986) 413

[Ärj85] Ärje, J. Äystö, H. Hyvönen, P. Taskinen, V. Koponen, J. Honkanen, A. Hautojärvi and K. Vierinen, Phys. Rev. Lett. **54** (1985) 99-101

[Äys01] J. Äystö, Nucl. Phys. A, submitted